JM PAPERS

Stability and bifurcation of dynamic contact lines in two dimensions

J.S. Keeler[1],†, **D.A. Lockerby**[2],†, **S. Kumar**[3],† **and J.E. Sprittles**[1],†

[1]Mathematics Institute, University of Warwick, Coventry CV4 7AL, UK

[2]School of Engineering, University of Warwick, Coventry CV4 7AL, UK

[3]Department of Chemical Engineering and Materials Science, University of Minnesota, Minneapolis, MN 55455, USA

The moving contact line between a fluid, liquid and solid is a ubiquitous phenomenon, and determining the maximum speed at which a liquid can wet/dewet a solid is a practically important problem. Using continuum models, previous studies have shown that the maximum speed of wetting/dewetting can be found by calculating steady solutions of the governing equations and locating the critical capillary number, Ca_{crit}, above which no steady-state solution can be found. Below Ca_{crit}, both stable and unstable steady-state solutions exist and if some appropriate measure of these solutions is plotted against Ca, a fold bifurcation appears where the stable and unstable branches meet. Interestingly, the significance of this bifurcation structure to the transient dynamics has yet to be explored. This article develops a computational model and uses ideas from dynamical systems theory to show the profound importance of the unstable solutions on the transient behaviour. By perturbing the stable state by the eigenmodes calculated from a linear stability analysis it is shown that the unstable branch is an 'edge' state that is responsible for the eventual dynamical outcomes and that the system can become transient when $Ca < Ca_{crit}$ due to finite-amplitude perturbations. Furthermore, when $Ca > Ca_{crit}$, we show that the trajectories in phase space closely follow the unstable branch.

Key words: contact lines, computational methods, bifurcation

† Email addresses for correspondence: jack.keeler@warwick.ac.uk, duncan.lockerby@warwick.ac.uk, kumar030@umn.edu, J.E.Sprittles@warwick.ac.uk

1. Introduction

Understanding the shape and evolution of the interface between a fluid, a liquid and a solid substrate is a classic problem in fluid mechanics and yet a remarkable number of open questions still remain (Semenov *et al.* 2011; Afkhami, Gambaryan-Roisman & Pismen 2020). There are two fundamental cases: an advancing contact line, where a liquid phase advances and 'wets' the solid (see figure 1*a–c*), and a receding contact line, where a liquid phase recedes and 'dewets' the solid (see figure 1*d–f*). Both experimental and theoretical studies (see e.g. Bonn *et al.* 2009; Snoeijer & Andreotti 2013) have shown that there is a critical contact-line speed relative to the solid, beyond which stability is lost and the system ceases to return to a steady state. In the case of an advancing contact line (see figure 1*c*) this instability is characterised by fluid entrainment (which in many practical cases is air entrainment) whilst for the receding contact line (see figure 1*f*) a thin liquid film is deposited on the solid. The principal aim of this article is to provide insight into this instability and understand the dynamics of the system near the critical speed.

The critical speed where the instability occurs is associated with a fold bifurcation in the steady solution structure (see e.g. Vandre, Carvalho & Kumar 2013; Kamal *et al.* 2019), which divides the steady solutions between a stable branch and an unstable branch (as seen in figure 2*a*; see Kuznetsov (1998) for a detailed mathematical description). For parameter values 'beyond the fold' there are no (known) two-dimensional steady states and the system must become transient and/or three-dimensional. In our system, the appropriate non-dimensional parameter associated with the speed of the solid is the capillary number, *Ca* (see next section for a precise definition). Whilst analysis of the unstable branch of solutions (which exists for parameter values 'below the fold') can reveal important information about transient behaviour, the focus of theoretical studies has been mainly to calculate and characterise only the stable steady solutions immediately up to the critical speed (see e.g. Eggers 2005; Chan, Snoeijer & Eggers 2012; Vandre *et al.* 2013; Sprittles 2015).

Interestingly, Chan *et al.* (2012) hypothesised that the set of unstable solutions represents, what they termed, 'effective dynamics', so that the unstable branch of the bifurcation curve guides time-dependent behaviour of the system. More specifically, when the capillary number is above its critical value ($Ca > Ca_{crit}$), and the speed of the contact line is measured relative to that of the solid, time-dependent trajectories closely match those obtained from the unstable branch of the steady system, as confirmed experimentally in Delon *et al.* (2007). Therefore, the unstable branch is not just an insignificant consequence of the fold bifurcation but provides unique insight into the system dynamics. Such an influence and importance of unstable states in fluid dynamics systems has been investigated in many different contexts, including shear flow (Eckhardt *et al.* 2008), droplets (Gallino, Schneider & Gallaire 2018), finite air bubbles (Keeler *et al.* 2019; Gaillard *et al.* 2020) and a slide-coating flow (Christodoulou & Scriven 1988). Indeed, as shown in figure 2(*b*), where the phase plane is sketched for a generic system with a stable ('attractor') and weakly unstable ('saddle-node') state, the unstable state can act as a separator of dynamical outcomes; its stable manifold is a dividing 'line' and its unstable manifold connects to the stable state. In this article we adapt these ideas from dynamical systems theory to the moving-contact-line problem, for the first time, to reveal the role of the unstable solutions. We calculate the bifurcation structure and stability properties of the steady solutions and relate these to time-dependent calculations in the subcritical ($Ca < Ca_{crit}$) and supercritical ($Ca > Ca_{crit}$) regimes.

We now provide some important background on moving contact lines. It is well known that the classical 'moving-contact-line paradox', as described in Huh & Scriven
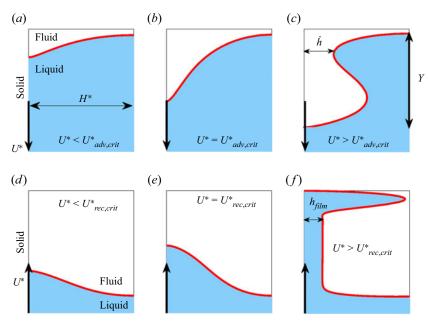
Figure 1. The moving contact-line problem in a channel geometry in a frame of reference that moves with the liquid. (a–c) The advancing contact-line problem. (d–f) The receding contact-line problem. In both cases, as the speed of the substrate, U^*, increases, the system is first stable (a,d), before the system becomes transient at a critical speed U^*_{crit} (b,e) and air entrainment (c) or thin-film formation (f) occurs. We denote the characteristic horizontal width of the fluid entrainment region in the advancing problem as $\hat{h}$ and the characteristic horizontal width of the thin film in the receding problem as h_{film}. The height of the interface, defined as the difference in heights of the left and right contact points, is denoted Y (cf. (2.21)). (a) Stable. (b) Critical. (c) Fluid entrainment. (d) Stable. (e) Critical. (f) Thin film.
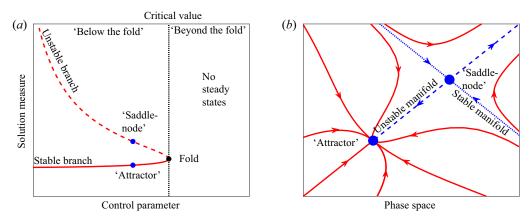

Figure 2. (a) A sketch of a typical fold bifurcation structure. A solution measure is plotted against a control parameter to form a solution curve. At a critical value, two branches – one stable (solid line) and one unstable (dashed line) – meet. The location of their intersection is known as a fold bifurcation. Beyond the critical value there are no (known) steady states. In our specific problem the control parameter is Ca and the solution measure is either the interface length or meniscus rise. (b) A generic two-dimensional phase plane for a parameter value less than the critical value with a stable state (an 'attractor' on the stable branch, see a), and a weakly unstable state (a 'saddle-node' on the unstable branch, see a). The unstable/stable manifolds of the saddle node are dashed/dotted respectively.

(1971), can be alleviated if there is slip near the contact point. Asymptotically, if this slip occurs in an inner region, as considered by Voinov (1976) and Cox (1986), then bending of the interface occurs in an intermediate region where viscous effects can cause the liquid–fluid interface to curve sharply. In this formulation, it is often assumed that the intermediate region connects to an outer region where the interface retains its static meniscus shape. The possible asymptotic matching of these regions has critical consequences and provides insight into the bifurcation structure of the steady solution space. In a series of remarkable articles (Eggers 2004*a*,*b*, 2005), it was shown, by solving a lubrication model for a liquid–vacuum system, how the curvature of the inner and outer regions can be asymptotically matched. For the advancing contact line this can be achieved for all values of *Ca*, but for the receding contact line, the matching fails when *Ca* is past some critical threshold, interpreted as (i.e. defining) Ca_{crit}. The bifurcation structure of the stable and unstable branches of the receding contact line was then fully described using matched asymptotics and bifurcation theory by Chan *et al.* (2012) for $Ca \ll 1$, and Ca_{crit} was determined to occur at a fold bifurcation.

The aforementioned analysis has been extended to general liquid–fluid systems, where the viscosity of the fluid phase is considered non-zero (Chan *et al.* 2013; Kamal *et al.* 2019; Chan *et al.* 2020) and also for the full Navier–Stokes equations (Vandre, Carvalho & Kumar 2012; Vandre 2013; Vandre *et al.* 2013). A key result from these studies is that, for the advancing contact line, the presence of viscosity fundamentally alters the bifurcation structure and a fold bifurcation appears at a finite *Ca*. Vandre *et al.* (2013) showed that, physically, this fold bifurcation in the advancing contact-line problem occurs when the horizontal air-pressure gradient matches the strength of the capillary-stress gradient near the contact point. It was also demonstrated that using the lubrication model, in both phases, poorly predicts Ca_{crit} when compared to the full Navier–Stokes equations for the advancing contact line (Vandre *et al.* 2012; Vandre 2013; Vandre *et al.* 2013). Other physical effects such as Marangoni flows, inertia, gravity and shear thinning/thickening were also found to preserve the fold bifurcation (Vandre *et al.* 2013; Liu *et al.* 2016*a*,*b*; Liu, Carvalho & Kumar 2017, 2019; Charitatos *et al.* 2020).

In the advancing case, the critical behaviour indicates the threshold at which fluid entrainment occurs where, experimentally, a three-dimensional saw-tooth pattern emerges as observed in a variety of different flow configurations, e.g. liquid films (Reysatt & Quéré 2006), drop impact (Thoroddsen *et al.* 2012; Pack *et al.* 2018) and plate penetration in a liquid bath (He & Nagel 2019). In the receding case, however, the fold bifurcation marks the onset of thin-film deposition (Snoeijer *et al.* 2006, 2008). Interestingly, despite the three-dimensional structures of air entrainment (He & Nagel 2019; He 2020), two-dimensional models appear to accurately predict the transition point, an observation which is yet to be understood (see e.g. Vandre *et al.* 2012; Sprittles 2017; Liu *et al.* 2019). Transversal three-dimensional perturbations have been considered for the receding contact line (Snoeijer *et al.* 2007) and the advancing contact line (Vandre 2013), both using a lubrication model, but a stability analysis using the full hydrodynamics equations has not yet been conducted.

In this article, we develop a computational framework and methodology that can quantitatively determine the stability of dynamic contact lines. To do so, we use ideas from dynamical systems theory to understand the effect of the stable/unstable states on the transient dynamics, considering both advancing and receding contact lines. We emphasise that the methodology we describe here can easily be extended to include different physics, including the effects of inertia, gravity, different slip conditions on the moving plate and different models that account for a velocity-dependent contact angle. We choose to

focus on understanding the qualitative transient behaviour, from a dynamical systems perspective, rather than attempting to include every physical effect in our model. Our analysis of two-phase contact-line stability focuses on steady-state solutions using a hybrid model; the liquid phase is modelled using the Navier–Stokes equations and the fluid phase is accurately modelled using a lubrication approximation (see Stay & Barocas 2003; Liu *et al.* 2016*a*,*b*, 2017; Sprittles 2017; Liu *et al.* 2019).

The structure of the article is as follows. In § 2 we discuss the hydrodynamic equations that describe the system. In § 3 we calculate the steady solution curves to determine the critical parameters associated with the loss of stability of the system. In addition, we perform a numerical linear stability analysis that reveals the significance of the unstable branch to the transient dynamics of the system. By treating the governing equations as a dynamical system we form a generalised eigenproblem that can be solved numerically to determine and quantify the stability of the solution branch. Next, in § 4, by solving a time-dependent initial value problem (IVP) numerically we are able to demonstrate that, far from having a passive role, the unstable branch represents, in the language of dynamical systems theory, the 'basin boundary of attraction' of the stable state. Furthermore, by examining the phase plane of the solution trajectory, we discover that the subsequent unsteady time evolution is intrinsically linked to the unstable branch and are able to confirm the prediction of Chan *et al.* (2012) that the receding contact line moves quasi-statically along the unstable branch. Viewing the trajectories through the lens of the phase plane allows us to understand if, and how, the system becomes transient when $Ca < Ca_{crit}$ and also provides criteria that could potentially enable suppression of this instability. Finally, in § 5, we discuss the implications of these results and some possible future research.

2. Governing equations

We now discuss the hydrodynamic model and the assumptions that allow us to derive an accurate simplified hybrid model that is used in the calculations thereafter. The following discussion applies to both the advancing and receding contact lines, although the demonstrative figures only show the advancing contact line.

2.1. *Full hydrodynamic model*

Motivated by the system used in Vandre *et al.* (2012), which is representative of an experimental system, we consider two-dimensional flow between two parallel plates, as shown in figure 1. In the following discussion we denote dimensional quantities using an asterisk. Two fluids of viscosity $\mu_{1,2}^*$, and density $\rho_{1,2}^*$, fill the channel bounded by two rigid plates which are separated by a fixed distance H^*; subscript 1 indicates the upper fluid (the fluid phase) and subscript 2 indicates the lower fluid (the liquid phase). In our system the left plate moves with constant speed in the y direction U^* and the right plate is stationary. For a receding contact line $U^* > 0$ and an advancing contact line $U^* < 0$. The fluid flow of each phase is governed by the two-dimensional Navier–Stokes equations. All speeds, lengths, pressures and times are scaled by U^*, H^*, $\mu_2^* U^*/H^*$ and H^*/U^* respectively. Finally, the viscosity ratio, denoted χ, is defined with respect to the liquid phase, i.e.

$$\chi = \mu_1^*/\mu_2^*, \tag{2.1}$$

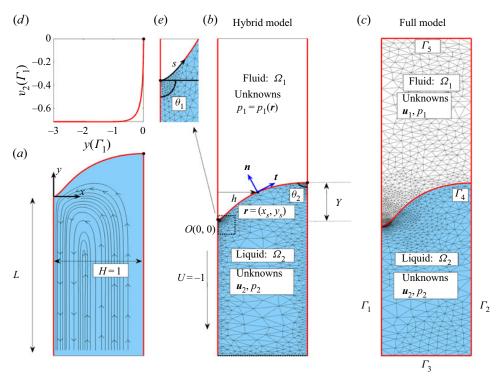and we assume that the upper fluid is less viscous, i.e. $\chi < 1$.

Figure 3. The computational domain for the hybrid and full models for an advancing contact line. The boundaries are denoted by Γ_i (labelled in c) with the origin centred on the contact line. (a) A typical streamline pattern for a steady solution in the hybrid model. (b) The computational domain for the hybrid model. In this model we solve for the velocity and pressure in the liquid domain, but only solve for the pressure of the fluid on the interface boundary, Γ_4. (c) The computational domain for the full model where the velocity and pressure fields are also solved in the fluid domain. (d) The vertical component of velocity along the moving plate, i.e. Γ_1. (e) The enlargement near the contact line shows the mesh refinement required to ensure that the flow field is sufficiently resolved.

As in previous studies (Sprittles & Shikhmurzaev 2011*a*,*b*; Vandre *et al.* 2012; Sprittles & Shikhmurzaev 2013; Vandre *et al.* 2013; Liu *et al.* 2016*a*,*b*, 2017, 2019) we apply the Stokes-flow approximation so that the Reynolds number, $Re = U^* H^* \rho_2^* / \mu_2^*$, is negligible and assumed zero; results in Vandre *et al.* (2013) show Re can have an influence at sufficiently high values but it does not qualitatively alter the conclusions. We assume that gravitational effects are negligible throughout. The non-dimensional computational domain is shown in figure 3(c). The coordinate system is centred on the contact point between the two fluids and the left (moving) plate. The boundary corresponding to the left plate is denoted Γ_1, the right plate Γ_2, the bottom Γ_3, the free surface Γ_4 and the top Γ_5. The fluid and liquid domains are denoted by Ω_1 and Ω_2 respectively. The Stokes-flow equations for the fluid velocity, $\boldsymbol{u}_i = (u_i, v_i)$, and pressure, p_i, in each phase can be written as

$$\chi \nabla^2 \boldsymbol{u}_1 = \nabla p_1, \quad \nabla \cdot \boldsymbol{u}_1 = 0, \quad \boldsymbol{x} \in \Omega_1 \quad \text{(fluid)}, \tag{2.2}$$

$$\nabla^2 \boldsymbol{u}_2 = \nabla p_2, \quad \nabla \cdot \boldsymbol{u}_2 = 0, \quad \boldsymbol{x} \in \Omega_2 \quad \text{(liquid)}. \tag{2.3}$$

On the left (moving) and right (stationary) plates, Γ_1 and Γ_2 respectively, we implement a Navier slip condition written as

$$\lambda(\boldsymbol{\tau}_i \cdot \boldsymbol{n}_p) \cdot \boldsymbol{t}_p = (\boldsymbol{u}_i - \boldsymbol{U}) \cdot \boldsymbol{t}_p, \quad \boldsymbol{x} \in \Gamma_1, \quad i = 1, 2, \tag{2.4}$$

$$\lambda(\boldsymbol{\tau}_i \cdot \boldsymbol{n}_p) \cdot \boldsymbol{t}_p = \boldsymbol{u}_i \cdot \boldsymbol{t}_p, \quad \boldsymbol{x} \in \Gamma_2, \quad i = 1, 2, \tag{2.5}$$

where $\boldsymbol{n}_p$ and $\boldsymbol{t}_p$ are the vectors normal and tangential to each plate respectively, $\boldsymbol{U} = (0, U)$ is the non-dimensional speed of the (moving) left plate (where U, in our dimensionless system, is ± 1, corresponding to the receding $(+)$/advancing $(-)$ problem) and λ is the non-dimensional slip length which, for simplicity, we assume to be the same in each phase (see Sprittles (2017) for potential extensions). We could choose different conditions that regularise the singularity at the contact line (Shikhmurzaev 2006), but, assuming the actual contact angle is unchanged, the details of the solution (i.e. the value of Ca_{crit}) are more sensitive to values of the slip-length parameter that arises in these models (in our case λ) than the actual form of the model (Dussan 1976). Thus, we would expect the results we obtain to be qualitatively similar to those obtained for a different slip model, although such slip models are easy to implement, if required. We choose a moderate value of $\lambda = 0.1$, and although quantitative details, i.e. the values of Ca_{crit} and other solution measures, will differ as we vary λ, we find that the transient behaviour and solution structure, as we describe later in the article, are qualitatively the same (cf. figure 7).

We choose to implement a Navier slip condition on the stationary plate for consistency and to ensure that the contact point on the stationary plate is allowed to move. However, we could fix $\boldsymbol{u}_i = 0$ on Γ_2 and get similar results (see e.g. Vandre *et al.* 2013; Liu *et al.* 2017) which corresponds to a pinned contact line. We also implement a no-penetration condition on each plate, i.e.

$$\boldsymbol{u}_i \cdot \boldsymbol{n}_p = 0, \quad \boldsymbol{x} \in \Gamma_1 \cup \Gamma_2, \quad i = 1, 2. \tag{2.6}$$

The stress tensor in each phase $\boldsymbol{\tau}_i$ is defined as

$$\boldsymbol{\tau}_i = -p_i \boldsymbol{I} + \delta_i(\boldsymbol{\nabla} \boldsymbol{u}_i + (\boldsymbol{\nabla} \boldsymbol{u}_i)^{\mathrm{T}}), \tag{2.7}$$

where $\boldsymbol{I}$ is the identity matrix and $\delta_1 = \chi$, $\delta_2 = 1$. We denote the unknown position of the interface, Γ_4, as $\boldsymbol{r} = (x_s, y_s)$ (see figure 3b) and assume a constant surface tension, γ^*, so that the dynamic boundary condition can be written as

$$\boldsymbol{\tau}_1 \cdot \boldsymbol{n} - \boldsymbol{\tau}_2 \cdot \boldsymbol{n} = \frac{1}{Ca}\kappa\boldsymbol{n}, \quad \boldsymbol{x} \in \Gamma_4, \tag{2.8}$$

where $\boldsymbol{n}$ is the normal of the interface pointing towards the fluid phase (see figure 3b), $\kappa = \boldsymbol{\nabla} \cdot \boldsymbol{n}$ is the curvature of the interface and $Ca = \mu_2^*|U|/\gamma^*$ is the capillary number. In addition to (2.8), we impose a kinematic condition on Γ_4, written as

$$\frac{\partial \boldsymbol{r}}{\partial t} \cdot \boldsymbol{n} = \boldsymbol{u} \cdot \boldsymbol{n}, \quad \boldsymbol{x} \in \Gamma_4. \tag{2.9}$$

We have to specify the angle that the interface makes on the left and right plates. These angles can be allowed to vary with the capillary number, slip length or other quantities but we choose the simplest approach and take these to be constant values, i.e.

$$\theta = \theta_1, \quad \text{on } \Gamma_1 \cap \Gamma_4, \tag{2.10}$$

$$\theta = \theta_2, \quad \text{on } \Gamma_2 \cap \Gamma_4. \tag{2.11}$$

It is straightforward to replace these conditions with equations involving Ca and other quantities, but this is not the focus of this article.

Finally, we implement fully developed flow conditions on the inflow and outflow boundaries:

$$u_i \cdot t_{inflow} = 0, \; x \in \Gamma_3 \cup \Gamma_5, \tag{2.12}$$

where $t_{inflow} = (1, 0)^T$, alongside a pressure drop across the domain so that

$$p_1 = 0, \; x \in \Gamma_5, \tag{2.13}$$

$$p_2 = p_{out}, \; x \in \Gamma_3. \tag{2.14}$$

The full hydrodynamic system is defined in (2.2)–(2.14) with the following infinite-dimensional state vector (denoted w) of unknowns:

$$w = [u_1, u_2, p_1, p_2, r]^T. \tag{2.15}$$

It is worth noting that we model the effect of varying the speed of the plate by varying Ca and that the non-dimensional slip length, λ, can be varied to investigate changes in physical channel width. Finally, as our primary interest is in understanding the transient behaviour, for simplicity, we set $\theta_1 = \theta_2 = \pi/2$ in all simulations. Therefore we have a set of control parameters,

$$Ca, \lambda, \chi, p_{out}, \tag{2.16}$$

that need to be specified in order to solve (2.2)–(2.14).

2.2. *Hybrid model*

The computational cost of the full model can be significantly reduced by solving the thin-film equations where they are valid (Oron, Davis & Bankoff 1997; Jacqmin 2004; Sbragaglia, Sugiyama & Biferale 2008), leading to a hybrid model (see Stay & Barocas 2003; Liu *et al.* 2016*a*,*b*, 2017, 2019; Charitatos *et al.* 2020) which approximately halves the complexity of the problem, as unknowns in the fluid phase are only computed on the interface. The difference of our approach from previous implementations is that our hybrid model takes into account time dependence so that stability can be probed and IVP calculations can be performed. A key assumption is that a typical horizontal distance in the fluid phase, when air entrainment occurs, is small when compared to the vertical height of the meniscus (i.e. $\hat{h} \ll Y$ in figure 1) so that the flow is approximately parallel, i.e. the cross-stream component of u_1 is small. The full derivation is discussed in Appendix A and the computational domain is shown in figure 3(*b*).

The effect of this reduction in the fluid phase is to replace a full two-dimensional description, given in (2.2), by a one-dimensional equation for the fluid pressure, p_1, on the interface only. This equation can be stated as

$$\frac{\partial r}{\partial t} \cdot n \pm \frac{1}{\chi} \frac{\partial Q_1}{\partial s} = 0, \quad Q_1 = \frac{1}{6} \frac{\partial p_1}{\partial s} h^3 + \frac{1}{2} A h^2 + B h, \tag{2.17a,b}$$

where h is the horizontal distance (i.e. x_s) from the left plate to the interface (see figure 3), Q_1 is the flux and the constants A and B are functions of χ, λ and u_2 and are given in Appendix A. The $\pm$ sign is used for the advancing (+)/receding (−) contact line. The fluid phase is coupled to the liquid phase through the applied traction given in (A6). We now have a system of partial differential equations (PDEs) described by (2.3)–(2.14) and (2.17a,b) with the infinite-dimensional state vector of unknowns:

$$w = [u_2, p_2, p_1(r), r]^T. \tag{2.18}$$

The hybrid model has been extensively validated for steady advancing contact-line problems against the full system and experiment (Liu *et al.* 2016*b*, 2019). We validate

the time-dependent hybrid model by comparing to the full hydrodynamic model in Appendix A. Finally we note that this approach is strictly only valid for the advancing contact-line problem but, as shown later, the receding contact-line problem is effectively a one-phase problem (cf. figure 7), and implementing the hybrid model for a receding contact line does not significantly change the value of Ca_{crit} (Appendix A).

2.3. *System parameters and integral measures*

We now describe additional system parameters and measures that will be useful in computing and describing the steady and time-dependent solutions. The pressure at the outflow boundary, p_{out}, is determined implicitly by an integral volume constraint acting on the liquid phase, i.e.

$$\iint_{\Omega_2} dV = V, \tag{2.19}$$

where V is the volume of the liquid domain (corresponding to the area of the computational domain). In our numerical calculations the positions of the contact points on the moving and stationary plates are both allowed to move so that (2.19) can be satisfied. For ease of presentation, we post-process and rescale the solution so that the origin is always at the contact point of the moving plate. In the calculations that follow we choose a value of V which is large enough for fully developed flow to occur near the outflow boundary, Γ_1. After careful experimentation we find that the solutions are independent of values of $V \geq 5$ that we choose.

For a fixed set of parameter values, as defined in (2.16), we calculate steady solution curves by setting the time derivatives in the governing equations to zero and then solving the resulting steady system. As we vary Ca, and then subsequently calculate a solution, a solution curve will be traced and a fold bifurcation will occur at the critical value of the capillary number, denoted Ca_{crit}. Whilst it is possible to trace a solution branch around the fold numerically by a pseudo-arclength continuation method (see e.g. Doedel 2007), we implement an alternative, bespoke approach. We expect the interface length, L, to increase monotonically as the curve is traced out around the fold and therefore it is a suitable candidate for a continuation parameter that allows us to calculate solutions smoothly around the fold. To achieve this, we let Ca become an unknown parameter that is determined implicitly by setting the total length of the interface, i.e.

$$\int_{\Gamma_4} ds = L. \tag{2.20}$$

This approach enables us to trace solution curves around the fold by incrementally increasing L and solving the system of equations, with Ca effectively determined by (2.20). We also emphasise that (2.19) and (2.20) are only implemented in steady calculations; the former constraint is unnecessary in time-dependent calculations as the second equation in (2.3) ensures volume is conserved, whilst the latter constraint is used as a means of tracing the solution curve.

Finally, when describing the steady solutions and time-dependent solutions we use the meniscus rise (more specifically, the vertical distance between the two contact lines) defined as

$$Y(t) = |y_s(s = L) - y_s(s = 0)| \tag{2.21}$$

as a convenient solution measure (as previously considered, for example, in Kamal *et al.* (2019); see figure 3 (in this article) for reference).

2.4. *Numerical method*

The governing equations are solved using the finite-element method from within the open-source oomph-lib object-orientated multi-physics library (Heil & Hazel 2006). The structure and implementation of our equations follow that of Sprittles & Shikhmurzaev (2013). Following multiplication of the equations by a test function, ψ, and then an integration over the domain, the boundary integrals that result from integration by parts require the traction to be specified on each of the boundaries. The dynamic condition, (2.8), and the Navier slip condition, (2.5), therefore can be implemented as a natural condition by these boundary integrals.

Special care has to be taken at the contact point. In other studies (Vandre *et al.* 2012, 2013; Liu *et al.* 2016*a*,*b*, 2017, 2019) the contact angle is imposed as an essential boundary condition at the expense of solving a component of the momentum equations at the contact point. We adopt the approach of Sprittles & Shikhmurzaev (2013) and impose the contact angle as a natural boundary condition on both the intersection of the free surface with the left plate (Γ_1) and the symmetry plate (Γ_2). We therefore introduce a field of Lagrange multiplier unknowns on Γ_1 and Γ_2 which are determined from the weak form of the no-penetration condition, (2.6). We refer the reader to Sprittles & Shikhmurzaev (2013) for a detailed description of this implementation (we adopt approach (B) in their nomenclature).

As is standard, the fluid velocities are interpolated using bi-quadratic shape functions and the pressure using linear continuous shape functions with Taylor–Hood triangular elements. We choose to mesh the liquid domain using an unstructured triangular grid (see figure 3*b*,*c*). The mesh is considered to be a fictitious pseudo-solid with the position of the nodes coming as part of the solution. The weak form of the kinematic condition, (2.9), is imposed as an essential condition and determines a field of Lagrange multipliers (not to be confused with the Lagrange multipliers in the previous paragraph) that act on the solid deformation equations which in turn determines the shape of the unknown interface, $\boldsymbol{r}$; see Sackinger, Schunk & Rao (1996) for more details. We note that this approach results in a large system of equations which is disadvantageous, but it allows for the interface to become highly deformed, as well as naturally handling time-dependent flow (where the domain could significantly change shape; cf. figure 1), which is difficult to achieve if the mesh is structured.

To solve the hybrid equation, (2.17*a*,*b*), it is convenient to introduce two fields of unknowns on the fluid interface, the pressure p_1 and flux Q_1, interpolated using quadratic shape functions. We solve two equations in their weak form:

$$\int_S (Q_1 - Q_C)\psi \, \mathrm{d}S = 0, \quad Q_C = \frac{1}{\chi}\left(Ah + \frac{1}{2}Bh^2 + \frac{1}{6}h^3\frac{\partial p}{\partial s}\right) \tag{2.22a,b}$$

and

$$\int_S \left(\frac{\partial \boldsymbol{r}}{\partial t}\cdot\boldsymbol{n} \pm \frac{\partial Q_1}{\partial s}\right)\psi \, \mathrm{d}s = 0. \tag{2.23}$$

Equation (2.22*a*,*b*) projects the flux from the lubrication equation onto the finite-element space and then (2.23) ensures mass is conserved in the fluid phase.

The resulting discretised equations are solved with Newton's method using the SuperLu numerical algebra package (Li 2005). For time-dependent calculations the solution is updated in time using a backwards-difference second-order Euler method (BDF2). A typical streamline pattern is shown in figure 3(*a*).

Around the contact line the interface becomes highly deformed due to viscous bending and the pressure and velocity gradients are large (see figure 3*d*,*e*). In steady calculations,

as $Ca \rightarrow Ca_{crit}$, we expect the number of elements required in the vicinity of the contact line to increase to ensure a smooth converged solution. We re-mesh the domain according to a ZZ error estimator (Zienkiewicz & Zhu 1992), which measures the discontinuity of strain-rate gradients between adjacent elements and interprets this as a measure for the local error. Typically we set a minimum error as 10^{-6} and a maximum error 10^{-3}, so that elements with error above this range get refined and those with error below this range get unrefined. We allow element sizes from 10^{-12} to 10^{-2} to accommodate these error estimates. We do not adapt the mesh at each calculation; rather we adapt the mesh based on the condition that

$$|\theta_1 - \theta_c| < 1.0°, \quad \theta_c = \text{atan}((y_2 - y_1)/(x_2 - x_1)), \tag{2.24a,b}$$

where θ_c is the computed angle based on (x_1, y_1) and (x_2, y_2), the coordinates of the nodes on Γ_4 directly at the contact line and immediately adjacent, respectively. The number of elements and their sizes are highly dependent on λ and Ca. As an illustrative example, for steady solutions at $\lambda = 0.1$, $\chi = 0.1$ and $V = 5$, the resulting mesh has $\sim 10^3$ triangular elements and $\sim 10^5$ discretised unknowns at $Ca = Ca_{crit}$.

3. Linear stability analysis

We now present the stability algorithm and results. Rather than perform a standard normal modes reduction to the Orr–Somerfeld equations (see e.g. Severtson & Aidun 1996), we take a more general approach that determines the modes as part of the solution. The analysis below is independent of the model, and although the results we present are from the hybrid model, these results also follow from the full model.

In both cases the PDE system can be written as

$$\mathcal{R}(\dot{w}, w) = 0, \tag{3.1}$$

where $\mathcal{R}$ is a nonlinear operator and $w(t)$ represents a state of the system at time t, given as a vector of all the unknowns (either (2.15) or (2.18)). The time derivatives, $\dot{w}$, appear in linear combinations in our system so we can decompose $\mathcal{R}$ into a linear mass operator, $\mathcal{M}$, that operates on the time derivatives in the problem and a nonlinear operator, $\mathcal{F}$, that operates on the spatial derivatives in the problem so that (3.1) becomes

$$\mathcal{R}(\dot{w}, w) \equiv \mathcal{M}(\dot{w}) + \mathcal{F}(w) = 0. \tag{3.2}$$

To proceed we write the state of the system, w, as a perturbation expansion, i.e.

$$w = w_\star + \varepsilon e^{\sigma t} g + O(\varepsilon^2), \tag{3.3}$$

where $w_\star$ is a base state only dependent on spatial variables, $\varepsilon \ll 1$ is a small parameter, g is an eigenmode that is dependent on spatial variables only and σ is the growth rate of the perturbation. The expansion in (3.3) represents a general class of perturbations that satisfy the boundary conditions of the problem and are in-plane perturbations; we are not extending to the third dimension, a problem we will discuss later.

Substituting (3.3) into (3.2) gives a series of problems that have to be solved at each order of ε. At leading order we have

$$\mathcal{F}(w_\star) = 0. \tag{3.4}$$

The solution, $w_\star$, is the steady state of the system. At first order we solve

$$[\sigma \mathcal{M}(w_\star) + \mathcal{J}(w_\star)] g = 0, \tag{3.5}$$

where $\mathcal{J}(w_\star)$ is the functional derivative of the nonlinear operator $\mathcal{F}$ applied at the steady state $w = w_\star$. Equation (3.5) is a generalised eigenvalue problem that can be solved to find

g and σ. The eigenspectrum of σ determines the stability of the steady solutions. If at least one of the spectrum of σ has a positive real part then the steady state is linearly unstable. Conversely if the entire spectrum lies in the left half of the complex plane then the solution is linearly stable. In general there will be an infinite number of these eigenmodes and thus we can write the linearised solution as

$$w_{lin}(t) = w_\star + \sum_{n=1}^{\infty} a_n g_n e^{\sigma_n t} + \text{c.c.}, \qquad (3.6)$$
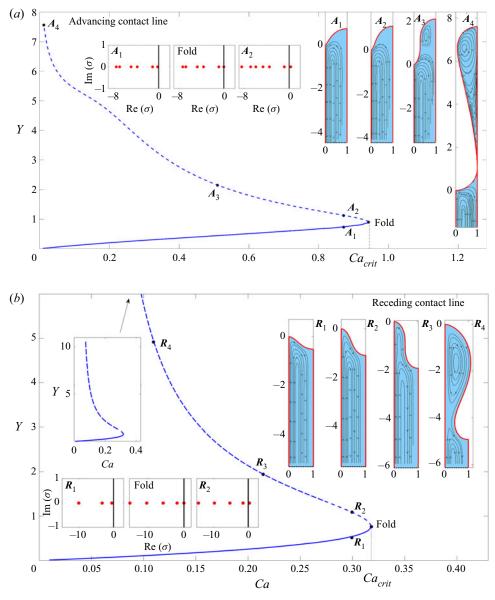
where c.c. denotes the complex conjugate and a_n are arbitrary constants set by the initial conditions. When the system becomes discretised, the operators $\mathcal{M}$ and $\mathcal{J}$ are represented by the mass matrix and Jacobian matrix, respectively. The mass-matrix representation of $\mathcal{M}$ is highly rank deficient as the only time derivatives occur at the fluid–liquid interface and special care has to be taken to ensure that the solution to (3.5) has converged. We use the Anasazi linear algebra library which is an iterative eigensolver that can solve highly rank-deficient eigenproblems (Heroux *et al.* 2003). As the spectrum has an infinite number of eigenvalues, the discretised spectrum will have a finite number of eigenvalues, proportional to the number of unknowns in the problem. We find a small subset of eigenvalues which have the largest real part as these will be the modes visible in the transient dynamics; large negative eigenvalues correspond to eigenmodes that decay very rapidly. We validate the calculations using a simplified lubrication model and present this in Appendix B.

3.1. *Stability of the solution branches*

We now discuss the bifurcation structure and the corresponding stability results of the advancing and receding dynamic contact-line problems. Figure 4 shows the bifurcation structures in a typical advancing case (figure 4*a*: $\chi = 0.1$, $\lambda = 0.1$) and receding case (figure 4*b*: $\chi = 0.0$, $\lambda = 0.1$). Notably, our focus here is on providing insight into the stability structure, rather than necessarily probing the precise values from experimental analyses, where the slip length could be far smaller and therefore typically require more computational resources. Previous works (Vandre *et al.* 2012) have shown that whilst changes in slip length can have a weak effect on Ca_{crit}, they do not qualitatively alter the physical mechanisms at play (similarly for smaller viscosity ratios, e.g. with a glycerol–air system).

The solution curves are shown in the (Ca, Y) projection of the solution space (see (2.21) for a definition of Y). The markers on the curve indicate specific solutions which are shown in the inset panels labelled A_1–A_4 for the advancing contact line, and R_1–R_4 for the receding contact line. In both the advancing and receding cases, as Y increases, the solution curve experiences a fold which separates the lower branch and upper branch. The eigenspectra are real and at the fold a single eigenvalue crosses the imaginary axis, as expected. The eigenspectra also indicate that the A_1/R_1 states (all eigenvalues in the left-hand Argand plane) are 'attractors' of the system and A_2/R_2 states (a single eigenvalue in the right-hand Argand plane, akin to a 'saddle-node' state in a two-dimensional dynamical system) are weakly unstable, as seen in figure 2(*b*), thus numerically confirming that the lower branch is stable (solid curve) and the upper branch is unstable (dashed curve).

The interface has an inflection point near the contact point. We measure the angle at the interface inflection point (to the downwards vertical) and, as is common, define this as θ_{app}; the apparent contact angle (Vandre *et al.* 2012; Liu *et al.* 2016*b*). Notably, as can be

Figure 4. Solution curves for the advancing (*a*) and receding (*b*) contact lines. The values of the control parameters are $\chi = 0.1$ (*a*) and 0 (*b*) and $\lambda = 0.1$ for both panels. Individual solutions are labelled on the curve and correspond to the inset panels with the same label. The solid/dashed lines sections of the curve are the stable/unstable branches, respectively. The smaller insets show the eigenspectra for the A_1/R_1 and A_2/R_2 solutions and at the fold. Solutions A_3/R_3 are the solutions where the inflection point on the interface first becomes parallel to the plate, i.e. when $\mathrm{d}x_s/\mathrm{d}y_s = 0$. In (*a*), A_4 is the solution just before the numerical calculations cease to converge. In (*b*), R_4 is the solution where the interface starts to 'overhang' the right plate. The top-left inset in (*b*) shows the bifurcation curve for larger Y.
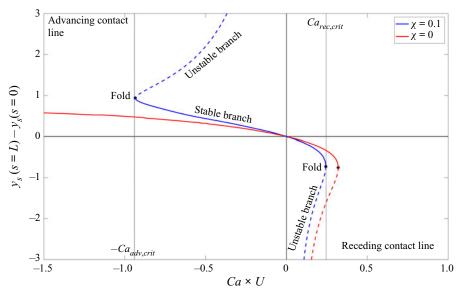
Figure 5. The advancing and receding steady solution curves for $\lambda = 0.1$ and $\chi = 0$ (red curves), $\chi = 0.1$ (blue curves). The horizontal axis is Ca scaled by $U = \pm 1$ and the vertical axis is $y_s(s = L) - y_s(s = 0)$, i.e. the signed version of Y. The critical Ca for each problem is denoted by a dotted line. The two problems are connected through the origin.

seen from solutions A_1, A_2 and R_1, R_2 in figure 4, $\theta_{app} < 180°$ not only on the stable branch, but also immediately after the fold on the unstable branch. This is consistent with the asymptotic results of Eggers (2004a), who shows that the solution at Ca_{crit} has $\theta_{app} \rightarrow 180°$ as $\lambda \rightarrow 0$. Consequently, for given $\lambda > 0$ we would expect to find that $\theta_{app} < 180°$ at Ca_{crit}. These findings are consistent with Sbragaglia *et al.* (2008).

Further up the unstable branch, see A_3, A_4 and R_3, R_4 in figure 4, $\theta_{app} = 180°$ and the interface develops a stationary point (i.e. $dx_s/dy_s = 0$). In the advancing case, the solution curve terminates when the interface touches the right plate and effectively appears to 'pinch off' off the fluid domain; see A_4. For the receding case, the calculations stop when the size of the computational domain no longer allows a converged solution.

The steady-solution curves of the advancing and receding contact-line problems, although treated separately in figure 4, are actually two halves of the same solution space. Figure 5 shows the connection for $\lambda = 0.1$, $\chi = 0$ and 0.1, where the signed meniscus rise, $y_s(s = L) - y_s(s = 0)$, is plotted against $Ca \times U$, where $U = \pm 1$ with $\pm$ corresponding to the receding (+)/advancing (−) problem. In this projection the advancing and receding curves occupy the second and fourth quadrants, respectively, and the location of the respective folds in each quadrant highlights that the advancing contact line only becomes unstable if $\chi \neq 0$, in which case $Ca_{crit,rec} < Ca_{crit,adv}$ (Marchand *et al.* 2012; Chan *et al.* 2013) and that, in general, $Ca_{adv,crit}$ and $Ca_{rec,crit}$ increase as $\chi \rightarrow 0$.

Finally, we note that in both cases the solution curve does not experience additional bifurcations as Y increases along the unstable branch. For a system where gravity is included it is known that within the lubrication approximation, the solution curve (for the receding contact line, at least) oscillates around a fixed value of $Ca = Ca^*$ (see Chan *et al.* 2012), experiencing multiple saddle-node bifurcations as $Y \rightarrow \infty$. Preliminary calculations show that, if gravity is included, the oscillations are also present in the advancing/receding hybrid system, although, for brevity, we do not show the results here.
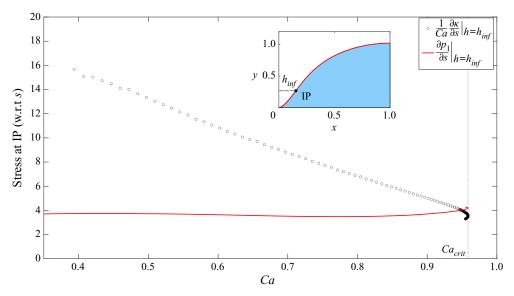
Figure 6. Comparison of the air-pressure gradient and the capillary-stress gradient for the steady solutions at the inflection point (IP) on the interface for the advancing contact-line problem. Parameter values are $\chi = 0.1$, $\lambda = 0.1$.

3.2. *Physical interpretation of the bifurcation*

As discussed in Vandre *et al.* (2013) for the advancing contact line, the fold occurs when the fluid-pressure gradients (fluid 1) are comparable to the capillary-stress gradients (see Vandre 2013) near the contact line, i.e. when

$$\frac{\partial p_1}{\partial s} \sim \frac{1}{Ca}\frac{\partial \kappa}{\partial s}. \tag{3.7}$$

This is because as $Ca \to Ca_{crit}$ the air-pressure gradients near the contact line will increase as the system seeks to 'pump' air out of the region near the contact line to maintain a steady state. Eventually these air-pressure gradients will exceed the capillary-stress gradients and the system will be unable to maintain a stable steady equilibrium. Figure 6 shows the evolution of the quantities on either side of (3.7) calculated at the inflection point for the advancing case. Here, one can see that the air-pressure and capillary-stress gradients balance close to Ca_{crit}, as seen by the intersection of the curves, which confirms the ideas of Vandre *et al.* (2013).

3.3. *Fold tracking*

We can take advantage of the fact that at the fold bifurcation the leading eigenvalue crosses the imaginary axis to develop an algorithm for finding Ca_{crit}. We augment the system with the additional constraint

$$\mathrm{Re}(\sigma_1) = 0, \tag{3.8}$$

and let another control parameter come as part of the solution. It is convenient to let the interface length, L, be determined by (3.8) so we are able to track the evolution of Ca_{crit} as another parameter, the viscosity ratio χ, for example, is varied. This is a robust way of tracking the fold without having to recalculate the solution curve for every set of parameters, as previously considered in Kamal *et al.* (2019) and Vandre *et al.* (2012).
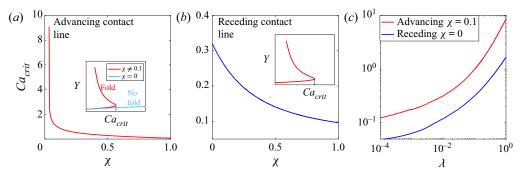
Figure 7. The evolution of the fold, and hence Ca_{crit}, as the relative viscosity χ (a,b) and the slip length λ (c) are varied. (a) The advancing contact line, $\lambda = 0.1$. As $\chi \to 0$, $Ca_{crit} \to \infty$ so that the fold in the bifurcation structure ceases to exist. The inset shows the generic bifurcation structure in the $\chi = 0$ and $\chi \neq 0$ cases. In the former case there is always a stable solution for the system to be attracted to. (b) The receding contact line, $\lambda = 0.1$. The fold exists for all viscosity ratios. For a given χ the bifurcation structure is shown in the inset. (c) Variation of Ca_{crit} as λ is varied for the advancing and receding problem (different colours) with $\chi = 0.1$.

If we vary χ and calculate Ca_{crit} we observe that the curve of the loci of Ca_{crit} does not itself experience any bifurcation, as seen in figure 7(*a,b*). In addition, we observe that the bifurcation structure also remains intact when the slip length, λ, is varied (see figure 7*c*). In fact, we note that the value of Ca_{crit} only changes relatively weakly as λ changes from $O(1)$ to $O(10^{-4})$. Therefore we expect the dynamics to be qualitatively similar (from a dynamical systems perspective) regardless of the slip length and provided $\chi \neq 0$.
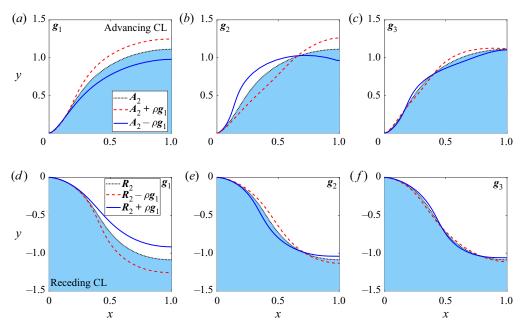
An important observation is that the advancing and receding cases differ significantly as $\chi \to 0$. For the advancing case, $Ca_{crit} \to \infty$ in this limit, whilst for the receding case it tends to a finite value. This indicates that the viscosity of the fluid phase has to be taken into account for the advancing contact line in order to describe the bifurcation structure. This feature has been identified before, in driven liquid filaments (Ledesma-Aguilar *et al.* 2011) and in plate-plunging experiments (Marchand *et al.* 2012). In contrast the receding contact line is essentially a one-phase problem, and the qualitative features of the bifurcation structure are the same regardless of the viscosity of the fluid.

3.4. *Eigenmode perturbations*

We now discuss the nature of the eigenmodes resulting from the stability analysis. The modes corresponding to the three leading eigenvalues of the unstable branch, i.e. σ_1, σ_2 and σ_3, are shown in figure 8. These eigenmodes correspond to the base states $w_\star = A_2, R_2$ in figure 4. In this figure the dotted profile indicates the steady interface shape and the coloured lines indicate the shape of the interface when it is perturbed by a single eigenmode, i.e.

$$w = w_\star \pm \rho g_i, \quad i = 1, 2, 3. \tag{3.9}$$

The dashed/solid curves correspond to the $+/-$ sign, respectively. The amplitude of the perturbation, ρ, is constrained so that the meniscus rise of the perturbation is no more than 10 % of the rise of the steady solution. Each successive mode intersects the steady interface at precisely one more location, in similarity to the form of the (sinusoidal) eigenmodes in a related lubrication model (see figure 20). Thus, the effect of adding higher-order eigenmodes to the steady state is to add extra corrugations to the interface and increase the overall length of the interface.

945 A34-16

Figure 8. The eigenmodes of the unstable branch. The steady profile is shown as the dotted line. (*a*–*c*) The leading eigenmodes, g_1, g_2, g_3, corresponding to the advancing $w_\star = A_2$ ($Ca = 0.873$, $\chi = 0.1$) solution in figure 4(*a*). (*d*–*f*) The leading eigenmodes corresponding to the receding $w_\star = R_2$ ($Ca = 0.3$, $\chi = 0$) solution in figure 4(*b*). In each case the eigenmodes cross the steady interface in successively more locations. The slip length is $\lambda = 0.1$.

Concentrating on the leading eigenmode alone, the action of adding a multiple of g_1 to a steady solution, i.e. using (3.9), stretches/shrinks the interface according to the $\pm$ sign with no additional corrugations. Figure 9(*a*) shows the stable A_1 and unstable A_2 states with solid lines and the perturbation from the A_1 state using (3.9) and $i = 1$ with dotted lines. This figure demonstrates that we can continuously 'stretch' the nonlinear stable state by increasing the strength of the perturbation, ρ, and can eventually achieve an interface with an identical value of Y to the unstable steady state and remarkably similar profile. This will have consequences, as discussed in the next section. We can also continuously deform the unstable branch in the same manner to match the interface of the stable branch. Therefore, we denote perturbations using the leading eigenmode only in (3.9) as 'stretch' perturbations.

In a physical experiment, perturbations will naturally emerge from the presence of 'noise' in the system causing fluctuations of the interface and contact line. We will take advantage of the stability analysis and mimic this 'noise' by using the higher-order eigenmodes in the perturbation, i.e.

$$w = w_\star + \sum_{i=1}^{N} \rho_i g_i, \tag{3.10}$$

where for the purpose of simple illustration we choose the amplitude coefficients, ρ_i, to be equal. Figure 9(*b*) shows the perturbed interface as the value of N increases from 1 to 10, which demonstrates that by increasing the value of N we are able to perturb the nonlinear steady interface with increasingly more corrugations or 'noise' in a systematic manner and hence be able to isolate specific geometric effects that act on the stability
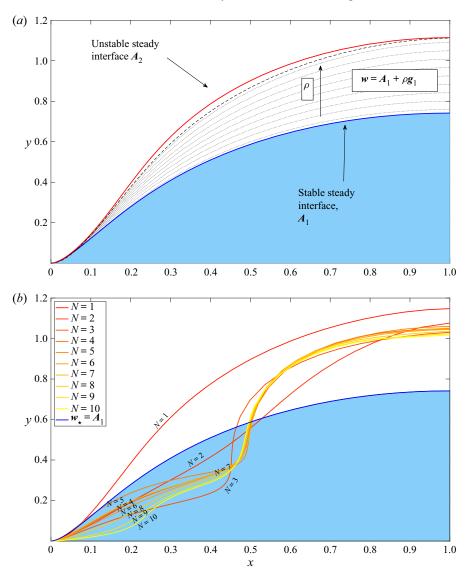
Figure 9. Perturbations of the advancing $w_\star = A_1$ state. (*a*) 'Stretch' perturbations. The lower solid curve is the stable interface and the upper solid curve is the unstable interface. The dotted curves are different strength perturbations of the stable state according to (3.9) with $i = 1$. The dashed curve corresponds to the perturbation which results in an identical value of Y as the A_2 state. (*b*) 'Corrugation' perturbations. The coloured curves are different strength perturbations of the stable state according to (3.10) for a fixed value of ρ and increasing N and the shaded region represents the nonlinear A_1 steady solution. Parameter values are $Ca = 0.873$, $\chi = 0.1$, $\lambda = 0.1$.

of the system (the first 10 modes are sufficient to analyse the response of the system as higher-order modes will decay rapidly). Strictly speaking, to model physical 'noise' would require performing a number of realisations with the values of ρ_i chosen randomly from a probability distribution, which must be chosen in some reasonable manner, ideas which we do not pursue further here. Henceforth, perturbations of the form in (3.10), i.e. a combination of leading-order and higher-order modes, are called 'corrugation' perturbations.

The two forms of perturbation discussed here, in our nomenclature the 'stretch' and 'corrugation' perturbations, are used in the next section to understand the subsequent time-dependent behaviour of the system after systematically applying a perturbation to a steady state.

4. Transient dynamics

Now that we have calculated the steady solution branches and quantified their stability, we attempt to answer the two questions of fundamental importance:

   (i) How do the steady states, stable and unstable, and the resulting bifurcation structure help us understand the time-dependent behaviour of the system when $Ca < Ca_{crit}$?

  (ii) What is the time-dependent behaviour of the system when we choose initial conditions beyond the fold, i.e. when $Ca > Ca_{crit}$?

To address these questions we solve the time-dependent hybrid PDE as an IVP. It is useful to define solution measures that will help visualise and aid the discussion. In our formulation Ca corresponds to the speed of the plate and not the speed of the contact point. It is therefore useful to introduce an 'effective' Ca, based on the contact-line speeds relative to the plate (as discussed in Chan *et al.* (2012)), which we denote $\overline{Ca}$ and is defined as

$$\overline{Ca} = Ca|U - U_{cl}|, \tag{4.1}$$

where $U = \pm 1$ is the non-dimensional speed of the plate, the $\pm$ sign corresponds to the advancing $(-)$/receding $(+)$ case and $U_{cl} = \mathrm{d}y_{cl}/\mathrm{d}t$ is the speed of the contact line. We remark that for steady solutions $U_{cl} = 0$, and hence $\overline{Ca} = Ca$ and the time-dependent phase-plane trajectories can be directly compared with the bifurcation structure in the $(\overline{Ca}, Y)$ plane.

We also introduce a system measure to quantify the size of the perturbation. Let the meniscus rise of a steady solution be $Y_\star$, where $\star$ indicates the base solution the perturbation is measured against. We can then define a quantity $\Delta(t, \star)$ that measures the deviation of the perturbation from the corresponding steady state at time t:

$$\Delta(t, \star) = Y(t) - Y_\star, \tag{4.2}$$

as demonstrated schematically in figure 10. If $\Delta(t, \star) > 0$ then the meniscus rise of the current state is larger than that of the steady interface indicated by $\star$ and vice versa if $\Delta(t, \star) < 0$ (see figures 10a and 10b, respectively).

4.1. *Perturbations from a steady-state IVP: $Ca < Ca_{crit}$*

We now consider the first question and look at the dynamics of the system when $Ca < Ca_{crit}$. Our methodology is to start at either the stable or unstable state and perturb it using either a 'stretch' or 'corrugation' eigenmode expansion, which we will consider separately. We then run a series of IVPs to examine the transient behaviour and eventual dynamical outcome.
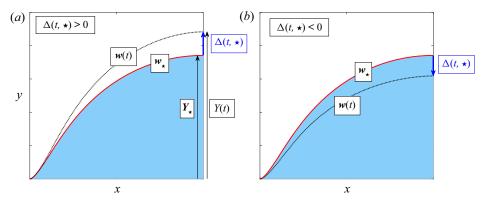
Figure 10. The perturbation measure. The solid curve in each panel is the interface of the base solution, $w_\star$, and the dotted curve represents the interface of the system at a given time, $w(t)$. (*a*) The system is in a state with $\Delta(t, \star) > 0$. (*b*) The system is in a state with $\Delta(t, \star) < 0$.

4.1.1. *'Stretch' perturbations*

For the 'stretch' perturbations, we use the leading eigenmode only, and set the initial conditions to be

$$w(t = 0) = w_\star \pm \rho \boldsymbol{g}_1. \tag{4.3}$$

Initially we concentrate on the advancing contact-line problem. Using the initial conditions stated in (4.3), small perturbations from the A_1 stable state (figure 4*a*) decay and the system (unsurprisingly) relaxes back to its stable configuration. Figure 11 demonstrates this by tracking the value of Y in time for two different perturbations, corresponding to $\Delta(0, A_1) < 0$ and $\Delta(0, A_1) > 0$, of the stable state near the fold (parameter values quoted in the caption). Furthermore, as seen in the insets on the right of figure 11, the decay rate excellently matches the value of the leading eigenvalue, σ_1, obtained from the linear stability analysis.

For the same parameter values, we can also perturb the A_2 unstable state (figure 4*a*) by its leading eigenmode, which is unstable. Figure 12(*a*,*b*) shows the time signal of Y as well as the phase-plane trajectories in the $(\overline{Ca}, Y)$ projection. This case is more interesting, and we see that if $\Delta(0, A_2) < 0$ (i.e. the perturbation 'contracts' the A_2 interface) then the system returns to the stable state (see figure 12*a*), whereas if $\Delta(0, A_2) > 0$ (i.e. a 'stretch') then entrainment of the upper fluid occurs (see figure 12*b*).

Similar outcomes occur for the receding contact-line problem. Perturbations, using the leading eigenmode, of the R_1 (figure 4*b*) stable state relax back to the stable equilibrium (results not shown). In contrast, figure 12(*c*,*d*) shows the time evolution of perturbations from the R_2 (figure 4*b*) unstable state, where for $\Delta(0, R_2) < 0$, the system relaxes back to the R_1 state. But if $\Delta(0, R_2) > 0$ then, unlike the advancing contact line where entrainment occurs, a thin film develops that grows in size at a linear rate as $t \to \infty$ as shown in figure 12(*d*).

These IVP calculations show that if we consider the class of perturbations representing 'stretches', using the leading eigenmode only, then the indicator of whether the system returns to the stable state is that meniscus rise of the initial perturbation is smaller than the meniscus rise of the unstable state, i.e. the condition for stability is

$$\Delta(0, A_2) < 0, \quad \text{advancing contact line,} \tag{4.4}$$

$$\Delta(0, R_2) < 0, \quad \text{receding contact line.} \tag{4.5}$$
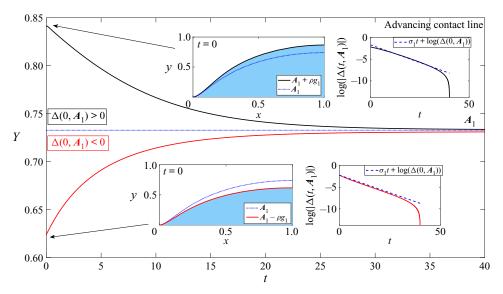
945 A34-20

Figure 11. Time-dependent perturbations of the advancing contact line using (4.3). This figure shows perturbations from the solution labelled A_1 in figure 4(a). The two different initial conditions are shown in the inset panels corresponding to the same colour lines in the main panel. Whether $\Delta(0, A_1) > 0$ or $\Delta(0, A_1) < 0$ the system relaxes back to the stable state. The inset panels on the right show the time signal of $\log(|\Delta(t, A_1)|)$ as compared to the predicted growth rate σ_1. Parameter values are $Ca = 0.873$, $\chi = 0.1$, $\lambda = 0.1$.

In the language of dynamical systems the unstable state represents the 'boundary of the basin of attraction' of the stable state, when considering simple stretches of the stable interface corresponding to perturbations using the leading eigenmode. The unstable state is therefore not just a trivial consequence of the steady bifurcation structure but also has an important role in dividing the phase plane into regions that have different transient dynamics.

Another important observation is that the calculation in figure 12(d), for the receding contact line, is consistent with the claim from Chan *et al.* (2012) that the solution curve represents the effective dynamics of the system 'in which the state of the solution moves quasi-statically along the solution curve'. In the receding case, the trajectory of the system in the phase space $(\overline{Ca}, Y)$ is qualitatively similar to the steady solution curve when plotted in the same diagram. The inset panels in figure 12(b,d) labelled 'Phase plane' show the steady solution curve and the trajectory of the system shown with an arrow. In the receding case, when $\Delta(0, R_2) > 0$ the trajectory closely follows the upper reaches of the unstable branch, whereas in the advancing problem this similarity does not occur. The comparison between the steady solution curve and the time-dependent trajectories is discussed in more detail in the next section. Finally, we note that the qualitative behaviour and conclusions that we have described are identical to the full model, as we show in Appendix C.

4.1.2. 'Corrugation' perturbations

We now concentrate on the 'corrugation' perturbations which arise from taking more eigenmodes in the perturbation expansion (3.10). As discussed in the previous section this class of perturbations includes higher modes, which we might reasonably expect in a noisy physical system. We choose the number of eigenmodes as $N = 10$ for
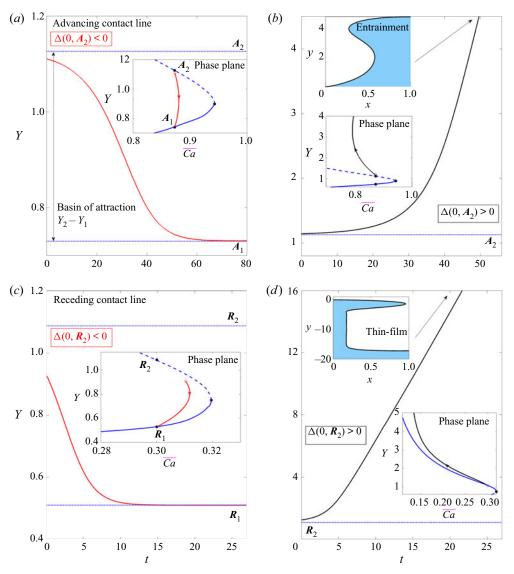
Figure 12. Time-dependent perturbations of the unstable branch using (4.3). (*a,b*) The advancing contact-line problem. (*c,d*) The receding contact-line problem. This figure shows perturbations from the solution labelled A_2/R_2 in figure 4. For both the advancing and receding contact line, when $\Delta(0, A_2) < 0$ the perturbation relaxes to the corresponding stable branch (*a,c*). When $\Delta(0, A_2) > 0$ the perturbation grows and in the case of the advancing contact line, entrainment occurs; see inset panel labelled 'Entrainment' in (*b*). For the receding contact line a thin film develops; see inset panel labelled 'Thin-film' in (*d*). The other inset panels show the phase plane in the $(\overline{Ca}, Y)$ projection. The initial conditions are marked as open circles, the system trajectory is marked with arrows and the steady bifurcation is shown without arrows. The unstable branch can be considered as the basin boundary of attraction of the stable steady state. Parameter values are $Ca = 0.873$, $\chi = 0.1$, $\lambda = 0.1$ for the advancing problem and $Ca = 0.3$, $\chi = 0$, $\lambda = 0.1$ for the receding problem.

computational efficiency. We set the initial condition of the system therefore as

$$w(t = 0) = w_\star + \rho \sum_{i=1}^{N} g_i + \text{c.c.}, \quad N = 10. \tag{4.6}$$

We concentrate solely on the advancing case and, as before, examine perturbations from the stable A_1 and unstable A_2 (figure 4a) states using the initial conditions prescribed in (4.6). Figure 13 shows the time-dependent results for incrementally increasing values of ρ in (4.6). Figure 13(a) shows trajectories in the (L, Y) phase-plane projection, where L is the total arclength of the interface. To help orient the trajectories we have added artificial axes which are centred on the unstable A_2 state.

After perturbing the A_1 state, initially the system 'smoothes' the corrugations, which is indicated by the decreasing value of L in the trajectories. Once these corrugations disappear, either the system becomes transient, and air entrainment occurs, or the system returns to the stable state. The dashed line between the A_1 and A_2 state is the response of the system if only the leading eigenmode is retained in the initial perturbation, as considered in the previous section on 'stretch' modes, which can be interpreted as the approximate unstable manifold of the A_2 state.

The nonlinear trajectories, i.e. the time-dependent solution to the hybrid system given in (2.3)–(2.14) and (2.17a,b) with initial conditions (3.10), all eventually collapse on the unstable manifold of the unstable A_2 state once the higher-order modes have sufficiently decayed, but, significantly, the combination of stable higher-order modes in the initial perturbation can cause transient behaviour, i.e. fluid entrainment, in the system, despite the corresponding eigenvalues being highly stable. This is in contrast to the linear response, i.e.

$$w_{lin}(t) = w_\star + \rho \sum_{i=1}^{N} g_i e^{\sigma_i t} + \text{c.c.}, \quad N = 10, \tag{4.7}$$

which will always decay back to the stable state (as the eigenvalues are all negative), as demonstrated in the inset diagram for a particular initial condition.

The unstable A_2 state, as indicated by a large circular symbol, plays a crucial role in the partition of behaviours. By examining the trajectories that explore the vicinity of the unstable branch in figure 13(a–c), it is not unreasonable to hypothesise that by continually refining the value of ρ in the initial perturbation the system would be able to stay in the vicinity of the unstable state for an arbitrary time period, where the dynamics of the system is dominated by the stable eigenmodes of the unstable branch. This behaviour is typically indicative of interpreting the unstable branch as an 'edge' state, commonly used to describe weakly unstable states in the transition to turbulence and other fluid dynamics problems (see Kerswell, Pringle & Willis (2014) for a description of an edge state). In these scenarios the weakly unstable 'edge' state acts as an 'edge' between two dynamical outcomes; in our problem it separates the system returning to the stable state or becoming transient.

The role of the unstable state is further emphasised in figure 13(d–f) for perturbations from the unstable A_2 branch. In figure 13(d) different colour trajectories correspond to whether a positive or negative ρ is chosen in the initial conditions given by (4.6), and figure 13(e,f) shows the initial conditions compared to the A_2 steady state. Again, the system outcomes are partitioned by the presence of the unstable state which 'deflects' the system to either relax back to the stable state or become transient so that entrainment occurs. We note that in this case if $\Delta(0, A_2) < 0$ (initial conditions in the lower half-plane of figure 13d) then the system will become transient which is in direct contradiction to the 'stretch' mode perturbations. These calculations demonstrate that L could be a more robust indicator of dynamical outcome; in this figure, all trajectories in the right-side (L, Y) plane (centred on the unstable state) eventually become transient as entrainment occurs.

To determine the exact regions in phase space where initial conditions becomes transient or return to the stable state requires knowledge of the stable manifold of the A_2 state (see
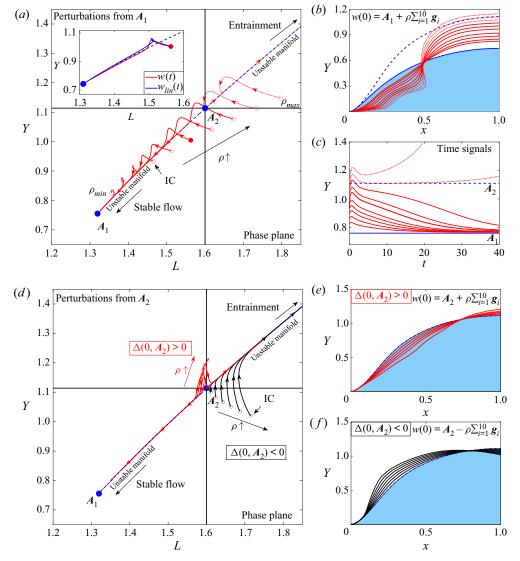
Figure 13. Time-dependent perturbations using the 'corrugation' perturbations. Perturbations from the solutions labelled in figure 4(*a*) using (4.6). (*a–c*) Perturbations from A_1. (*d–f*) Perturbations from A_2. (*a,d*) Time-dependent trajectories in the in the (L, Y) phase-plane projection. Initial perturbations (IC) are denoted by open circles and steady states by large solid circles. The dashed blue lines indicate the unstable manifold of the A_2 state and the solid black lines are artificial axes centred on the unstable A_2 state. (*a*) Each red curve indicates a time-dependent trajectory with a different value of increasing ρ, as indicated by the black arrow, the initial conditions with minimum and maximum ρ have been labelled. The solid trajectories correspond to initial perturbations that return to the steady state and dotted trajectories correspond to trajectories that result in entrainment. The inset shows the linear response given in (3.6) for a particular initial condition marked with a filled circle in the main panel. (*b*) The initial interfaces of the trajectories shown in (*a*) are shown as solid lines and the A_1 and A_2 steady states are shown using the shaded area and a dashed line, respectively. (*c*) The corresponding time signals of Y for the trajectories shown in (*a*). (*d*) Red/black curves indicate trajectories with initial conditions $\Delta(0, A_2)$ positive/negative, respectively. (*e,f*) The initial conditions corresponding to the trajectories in (*d*) with the unstable state indicated by the shaded area. Parameter values are $Ca = 0.873$, $\chi = 0.1$, $\lambda = 0.1$.

figure 2*b*). In our high-dimensional system of PDEs, the calculation of the stable manifold of the A_2 state is a non-trivial task (see e.g. Krauskopf *et al.* 2005) which we do not pursue here.

4.1.3. *Physical significance of the perturbations*

We now relate these results to the physical system. Firstly, we make the key observation that the system is able to experience instability for $Ca < Ca_{crit}$ due to finite-amplitude perturbations of the stable state. Furthermore, these results suggest that the system is susceptible to instability caused by perturbations that increase the total arclength; corrugations, representing 'noise', can be just as dangerous as perturbations that increase the meniscus rise. Given that noise is a ubiquitous phenomenon in physical systems we would expect to see this realised in a system with $Ca < Ca_{crit}$. Secondly, the extent to which we are able to perturb the stable A_1/R_1 state so that the system remains stable is dictated by the information encoded in the unstable A_2/R_2 steady state, in particular whether the perturbation causes the interface length or meniscus rise to increase beyond that of the unstable steady state. A consequence of this is that the closer Ca is to Ca_{crit} (from below), the smaller is the finite amplitude required to cause the system to become transient, as the stable and unstable branches are increasingly approaching each other.

We can be more precise and approximate the 'size' of the maximal stretch perturbation that maintains a steady contact line as a function of $Ca - Ca_{crit}$. Locally to the fold, the bifurcation curve will take the form

$$Ca - Ca_{crit} = a_1(Y - Y_{crit})^2 + a_2(Y - Y_{crit})^3 + \cdots , \qquad (4.8)$$

where Y_{crit} is the meniscus rise at the fold and a_i are constants that can be determined by, for example, normal-form reduction methods (Kuznetsov 1998). Therefore, close to the fold, the 'length' of the basin boundary is approximately equal to the vertical distance between the stable and unstable branches and is approximately

$$Y_2 - Y_1 = \sqrt{\frac{2}{a_1}} |Ca - Ca_{crit}|^{1/2}. \qquad (4.9)$$

As a conclusion, finite disturbances from the steady stable state potentially lead to instability before that interface might become transient otherwise (due to a lack of steady state). Minimising ambient disturbances and minimising fluctuations in Ca would help maintain a stable interface for higher Ca. The physical mechanisms underlying the observations are not straightforward to address due to the highly nonlinear nature of the problem. Moreover, three-dimensional perturbations will likely be important in practice and introduce additional physical mechanisms. Such three-dimensional calculations are exceedingly challenging and are currently the focus of ongoing research, so we defer a detailed study of physical mechanisms for future work.

4.2. *Dynamics 'beyond' the fold:* $Ca > Ca_{crit}$

We now turn our attention to starting the system from rest with a flat interface beyond the fold, i.e. $Ca > Ca_{crit}$, so that we are able to answer the second question stated at the start of § 4. The initial condition is

$$w(t = 0) = [u(0), p(0), p_1(0), r(0)]^{\mathrm{T}} = [0, 0, 0, (x_s, 0)]^{\mathrm{T}}. \qquad (4.10)$$

For values of Ca exceeding the critical value there are no (known) steady states which can influence the system, unlike in the previous section. For the advancing case, the system
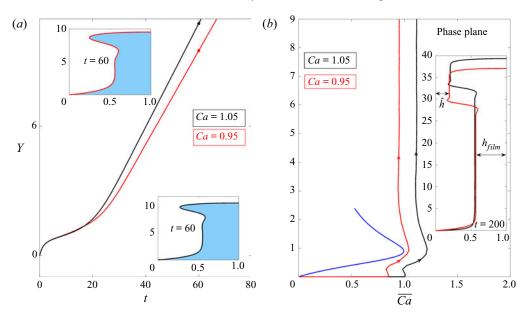
Figure 14. Time-dependent evolution for an advancing contact line when $Ca > Ca_{crit}$ and the system is at rest initially for $\lambda = 0.1$, $\chi = 0.1$. The different colour curves indicate different values of $Ca = 0.95, 1.05$. (*a*) The time signal of Y with interface profiles at the indicated times in the inset. (*b*) The trajectories (curves with arrows) in the $(\overline{Ca}, Y)$ phase-plane projection compared with the steady bifurcation curve (curve without arrows). The inset compares the interface profiles for each Ca at $t = 200$.

becomes transient with entrainment occurring, as shown in figure 14 where the time signal of Y is measured along with time snapshots of the interface at the times indicated for $Ca = 0.95, 1.05$. We emphasise that the system is not attracted to a different steady state of the system that may exist and we are unable to find any additional steady states beyond the fold bifurcation. There are two distinct length scales present in the interface profile for sufficiently large times. The width of the fluid entrainment, $\hat{h}$, and the width of the thin film, h_{film}, appear to be weakly dependent on Ca as shown by the inset of figure 14(*b*). These results are consistent with recent experimental work (He & Nagel 2019), but we leave a detailed analysis of the thickness of these entrainment regions, and their dependence on system parameters, to a future study; our focus is on the broad dynamical outcome, rather than the fine details of the solution. We do, however, remark that the hybrid model shows excellent promise in being able to predict the width of these films.

For the receding case, a thin film develops. Figure 15(*a*) shows the time signals of Y in the receding case when $Ca = 0.4, 0.5 > Ca_{crit}$. The system, although not approaching a steady state, forms a coherent structure whose meniscus rise grows at a constant velocity, independent of Ca, similar to the structure seen in figure 12(*c*). Unlike the advancing case, the time-dependent trajectories and the steady solution curve for the receding problem, when plotted in $(\overline{Ca}, Y)$, are qualitatively similar. Figure 15(*b*) also compares the actual interface profiles for the time-dependent calculation and the corresponding steady solution for the same value of Y (insets). It is striking how close the two corresponding interface profiles are, although we note that in the time-dependent case the horizontal height of the inflection point is smaller than that of the steady solution in all of the cases. This again
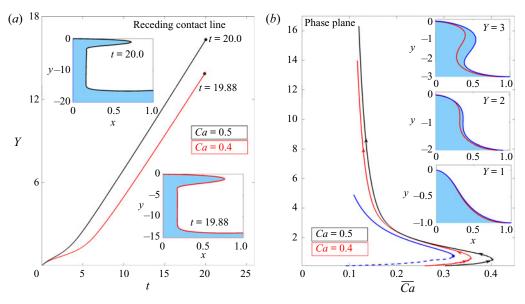
Figure 15. Time-dependent evolution for a receding contact line when $Ca > Ca_{crit}$ and the system is at rest initially for $\lambda = 0.1$, $\chi = 0$. The different colour curves indicate different values of $Ca = 0.4, 0.5$. (*a*) The time signal of Y with the final interface profiles in the inset. (*b*) The trajectories (curves with arrows) in the $(\overline{Ca}, Y)$ phase-plane projection compared with the steady bifurcation curve (curve without arrows). The inset panels compare the interface profiles for the time-dependent evolution (red) and the steady solution branches (blue) at the same values of $Y = 1, 2, 3$ for the $Ca = 0.4$ case.

shows compelling evidence that in the receding contact-line problem the unsteady solution branch represents the effective dynamics of the system.

In both the advancing and receding contact-line problems, the system trajectory approaches a fixed value of $\overline{Ca}$ as $t \to \infty$. For the advancing contact line, the limiting meniscus rise velocity is dependent on Ca (see slopes in figure 14*a*) so that the trajectories approach a limiting value of $\overline{Ca}$ which depends on Ca (see figure 14*b*). However, for the receding contact line, the limiting value of $\overline{Ca}$ appears to be almost independent of Ca (see figure 15*b*), indicating the contact-line region and the thin-film region are essentially de-coupled by this point. This would mean that if, after a thin film has developed, we slow the plate speed so that $Ca < Ca_{crit}$, the contact line would continue to move upwards and only the thin-film thickness, which is dependent on Ca according to a Landau–Levich-type law (Landau & Levich 1988), would change. Figure 16 shows this situation, where the trajectory in the $(\overline{Ca}, Y)$ plane of a receding contact-line IVP initially starting at rest when $Ca > Ca_{crit}$. Once a film is developed we instantaneously change the value of $Ca < Ca_{crit}$, once Y is large enough (we choose $Y = 6$ for convenience) and observe the contact line continuing to rise, whilst the thin film becomes smaller, adjusting to the changed value of Ca.

We do not have a concrete physical explanation for why the trajectories and steady bifurcation curve closely match one another for the receding contact line. From a dynamical systems perspective it is possible that the stable manifolds of the unstable branch persist as $Ca > Ca_{crit}$ and that the system is constantly being 'attracted' by the remnants of the stable manifolds. This is, of course, speculation, and we leave this aspect as a challenge for future work.
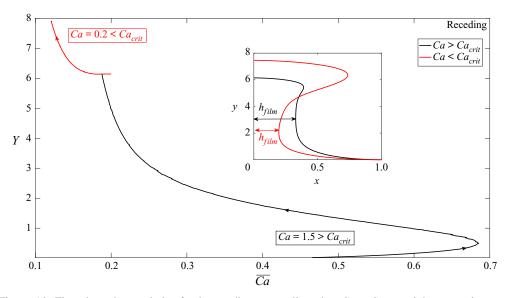
Figure 16. Time-dependent evolution for the receding contact line when $Ca > Ca_{crit}$ and the system is at rest initially. Once a film has formed and $Y = 6$, we set $Ca < Ca_{crit}$, as indicated in the figure by different colour trajectories and interface profiles. Other parameter values are $\lambda = 0.1$, $\chi = 0.0$.

5. Discussion

We have developed a time-dependent hybrid model and utilised ideas from dynamical systems theory to investigate the advancing and receding contact-line problems. By solving a generalised eigenproblem numerically and performing IVP simulations we have demonstrated that far from being passive, the unstable branch of the bifurcation structure plays a subtle role in the underlying time-dependent behaviour, from a dynamical systems perspective.

By perturbing the stable branch using the eigenmodes we have demonstrated that the unstable branch represents the basin boundary of attraction of the stable solution and it has a profound effect on the eventual evolution of the system. We have demonstrated that perturbations that cause the interface to stretch are robust, in that provided the stretch does not exceed that of the unstable branch the system returns to the stable state. In contrast, perturbations that increase the overall length of the interface by adding 'corrugations' are also dangerous and the system can become transient, despite these 'corrugations' corresponding to stable eigenmodes, as indicated by figure 13(*d–f*). This information may be helpful in physical systems as a means of flow control, as knowledge of the structure of the unstable eigenmodes may enable us to stabilise the system using suction/injection techniques. We also note that in physical experiments, estimates of Ca_{crit} should be interpreted as a lower bound, because in practice fluctuations may cause the system to become transient, despite a stable state existing, which has implications in real-life control of fluid systems.

We note that the perturbations we have considered here are purely theoretical eigenmode perturbations and it would be of interest to examine the stability of the contact line when physically perturbed by, for example, the surface defects on the moving substrate. This is part of the authors' current research.

In addition, for the receding case, by performing time-dependent calculations we have shown that trajectories in phase space qualitatively match the steady bifurcation structure.

945 A34-28

The solution curve describes what Chan *et al.* (2012) termed the 'effective dynamics' of the system. The bifurcation structure remains structurally stable (i.e. the stable–fold–unstable branch structure does not change) as χ and λ are varied (see figure 7), and hence we predict the overall qualitative behaviour to be similar, i.e. the unstable branch is generically the basin boundary of attraction for systems of this nature.

Gravitational and inertial effects can easily be added to the model and it is interesting to consider what effect these would have on the bifurcation structure and stability analysis. We have already performed some preliminary calculations incorporating gravity and have found that the bifurcation structure experiences the same multiple saddle-node bifurcations as predicted by the lubrication model (Chan *et al.* 2012). Our preliminary analysis shows that the entire upper branch past the first saddle-node bifurcation is unstable, but we have not pursued this in detail and leave this for future research. For inertial effects, we could expect other types of bifurcations, including Hopf bifurcations, which would introduce complex eigenvalues to the spectrum of σ and lead to more complex transient behaviour. We also leave this avenue for future research.

We emphasise that the computational stability algorithm and methodology presented here are independent of the governing equations that are chosen, even if the results differ. The system we decide to analyse is applicable to a wide range of physical settings where gravity and inertia play a minimal role (see e.g. Ledesma-Aguilar *et al.* 2011) but these physical effects, and even different contact-line physics such as that which molecular kinetic theory proposes (see e.g. Blake 2006), can easily be incorporated into our computational framework. In fact, any dynamic wetting system that can be written in the form

$$R(\dot{w}, w) = 0, \tag{5.1}$$

where R represents a dynamic wetting model that is appropriate for the physical situation with a set of state variables given by w, is amenable to the analysis that we have described.

In our model, we choose the simplest approach and set the contact angle to be constant. It is hotly debated whether this is indeed physically realistic and whether the actual contact angle varies or whether all dynamics of the angle are 'apparent'. A natural extension to the model would be to investigate the effect of having a contact angle that is dependent on the velocity of the plate, such as that proposed by molecular kinetic theory (see e.g. Blake 2006; Fernández-Toledano, Blake & Coninck 2021) or the interface formation model (see Shikhmurzaev 2007). Provided the bifurcation structure remains intact (i.e. stable–fold–unstable) then we predict the dynamics will be qualitatively the same. This is the subject of another article where we apply the hybrid model and stability algorithm developed here to account for a *Ca*-dependent contact angle observed in molecular simulations (Keeler *et al.* 2021).

For the advancing contact line, the instability manifests itself as fluid entrainment and for the receding contact line, a thin film and a capillary ridge form. The instability in this study is taken in a two-dimensional context but it is well known that the 'saw-tooth' patterns that emerge in an unstable advancing contact line are intrinsically three-dimensional. An intriguing extension to our model would be to consider transverse perturbations of the advancing contact line in the third dimension and perform a stability analysis, similar to our approach here. This has been done before in the receding case (Snoeijer *et al.* 2007) and the advancing case (Vandre 2013) using a lubrication model, but the time-dependent hybrid model developed here is a perfect testing ground for a three-dimensional calculation as the computational cost is relatively small compared with the full model, and we are also able to fully account for the two-dimensional (lubrication-violating) velocity in the liquid. This direction of research is currently being developed.

Declaration of interests. The authors report no conflict of interest.

Author ORCIDs.
- J.S. Keeler https://orcid.org/0000-0002-8653-7970;
- D.A. Lockerby https://orcid.org/0000-0001-5232-7986;
- S. Kumar https://orcid.org/0000-0003-0829-6355;
- J.E. Sprittles https://orcid.org/0000-0002-4169-6468.

Author contributions. J.S.K. performed all numerical simulations. All authors contributed equally to analysing data and reaching conclusions, and in writing the paper.

Data availability statement. The data that support the findings of this study are openly available in figshare at https://doi.org/10.6084/m9.figshare.17277812.

Appendix A. Derivation of hybrid model

As the flow is approximately one-dimensional, using a lubrication approximation, the momentum equations of the fluid phase are known to reduce (Oron *et al.* 1997) in our case to

$$\frac{\partial p_1}{\partial x} = 0, \quad \frac{\partial p_1}{\partial y} = \chi \frac{\partial^2 v_1}{\partial x^2}, \tag{A1}$$

so the pressure in the fluid phase is a function of y only and a straightforward two-fold integration of the momentum equation in (A1) yields an expression for v_1, i.e.

$$v_1 = \frac{1}{\chi}\left(\frac{1}{2}\frac{\partial p_1}{\partial y}x^2 + Ax + B\right), \tag{A2}$$

where A and B are constants of integration. We impose the Navier slip condition on $x = 0$ and impose continuity of velocity at the interface boundary, denoted by $x = h$, as in figure 3(*c*). These conditions determine A and B:

$$A = \frac{B - U\chi}{\lambda}, \quad B = \frac{\chi(Uh + \lambda v_2) - \frac{1}{2}\lambda(\partial p_1/\partial y)h^2}{\lambda + h}, \tag{A3a,b}$$

where v_2 is the vertical component of velocity of the lower fluid and p_1 is the upper fluid pressure, both evaluated at the interface. We have now determined the vertical velocity in the fluid phase in terms of the (as yet) unknown pressure gradient $\partial p_1/\partial y$ on the interface.

We now use conservation of mass to form an equation that determines the pressure in the fluid at the interface. The conservation equation, (2.2), can be written as

$$u_1 - \frac{\partial h}{\partial y}v_1 \pm \frac{1}{\chi}\frac{\partial}{\partial y}\left(\frac{1}{6}\frac{\partial p_1}{\partial y}h^3 + \frac{1}{2}Ah^2 + Bh\right) = 0, \tag{A4}$$

where the $\pm$ sign is used for the advancing (+)/receding (−) contact line. As typical horizontal length scales are small compared with vertical distances in the fluid when entrainment occurs, i.e. $\hat{h}/Y \ll 1$ (see figure 1*c* for illustrations of $\hat{h}$ and Y), then the arclength along the interface, s, measured from the contact point (see figure 3*e*) is $s = y + O(\hat{h}/Y)$. Therefore we can replace derivatives with respect to y with derivatives

with respect to s which means the first two terms above become $\boldsymbol{u}_1 \cdot \boldsymbol{n}$. The arclength parameterisation is preferable, as it allows the interface to become multi-valued in calculations. Using the kinematic condition (2.9) at the interface means that (A4) becomes

$$\frac{\partial \boldsymbol{r}}{\partial t} \cdot \boldsymbol{n} \pm \frac{1}{\chi} \frac{\partial Q_1}{\partial s} = 0, \quad Q_1 = \frac{1}{6} \frac{\partial p_1}{\partial s} h^3 + \frac{1}{2} A h^2 + Bh, \quad (A5a,b)$$

as stated in the main text. This equation determines the evolution of the pressure in the fluid phase on the interface. We set $p_1(s = L) = 0$ and $Q_1(s = 0) = 0$ to ensure the system is well-posed. The velocity in the fluid phase can be recovered using (A2). In this formulation, the equations in the liquid phase are coupled to (A5a,b) due to the presence of v_2 in the definition of the constant A. Furthermore, we couple the pressure and velocity in the fluid phase to the liquid phase through the dynamic boundary condition, i.e.

$$\boldsymbol{\tau}_1 \cdot \boldsymbol{n} = -p_1 \boldsymbol{n} - \chi \frac{\partial v_1}{\partial x} \boldsymbol{t}, \quad \boldsymbol{x} \in \Gamma_4, \quad (A6)$$

where $\boldsymbol{t}$ is the tangent along the direction of the arclength s (see figure 3b), which is standard when using a thin-film approximation (Oron *et al.* 1997).

A.1. *Justification of the model*

We now discuss the justification of the hybrid model. For small Ca the hybrid model's slender geometry approximation is not valid, but because in this regime upper fluid stresses are small compared with the capillary stress (i.e. the fluid is dynamically passive), the difference between the hybrid and full model is small. In contrast, in the large-Y regime, the geometry is genuinely slender in the upper fluid phase and a hybrid model is justified and we expect the difference again to be small. However, there are cases when the hybrid model loses accuracy. For example, when the upper fluid is a liquid of similar viscosity its stress on the interface is significant even at moderate Ca and the geometry is not always slender – clearly such cases require the full model, although figure 17, which shows a comparison of steady solutions of the receding contact line between the hybrid (solid lines) and full (circular markers) models for $\lambda = 0.1$ and $\chi = 0.1$, demonstrates that even at $\chi = 0.1$ agreement between the models is reasonable.

The hybrid model has been extensively validated for steady solutions of the advancing contact-line problem, over a wide range of χ (Liu *et al.* 2016b), and has also shown impressive agreement with curtain-coating experiments (Liu *et al.* 2019). Here, we show that the time-dependent hybrid model is consistent with the full model by performing a series of time-dependent IVP calculations starting the system from rest ($\boldsymbol{u}_i = \boldsymbol{0}$) with a flat interface. If we choose $Ca < Ca_{crit}$ we expect the system to eventually relax to a stable state. As $\chi \to 0$ the full model and the hybrid model should converge, because the pressure in fluid 1 reduces to $p_1 = $ constant so that the hybrid and full models are described by identical equations. Figure 18 shows the time signal of the meniscus rise, Y, for different viscosity ratios (different colours) for the full model (dotted lines) and the hybrid model (solid lines). In all cases the interface eventually relaxes to a stable state, as shown by the time signals in the main figure. It is also clear that for the smallest value of χ in the figure the full and hybrid models are virtually indistinguishable. This is because for small χ, the fluid only has an influence on the liquid in thin films (where the liquid phase has an approximately constant height, $\hat{h}$; see figure 1c) in front of the contact line, and this is where the lubrication model is valid. In contrast, at moderate χ the influence of the fluid is felt everywhere, the films are thicker/non-existent and this approximation loses accuracy. In other words, this approximation works best when the fluid is a gas.
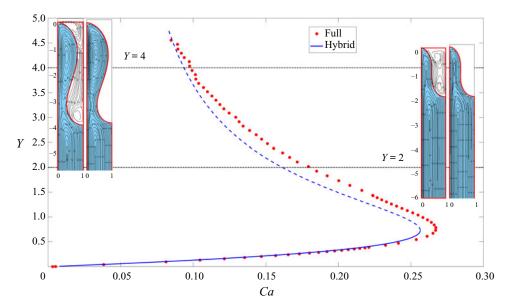
Figure 17. Steady bifurcation curve of the receding hybrid and full model when $\lambda = 0.1$, $\chi = 0.1$. The horizontal axis is Ca and the vertical axis is the meniscus rise, $Y = |y_s(s = L) - y_s(s = 0)|$. The solid markers are the full model solutions and the solid/dashed lines are the corresponding hybrid model results. The insets show the comparison of the interface and streamlines in the full and hybrid models when $Y = 2$ (right-hand insets) and $Y = 4$ (left-hand insets).
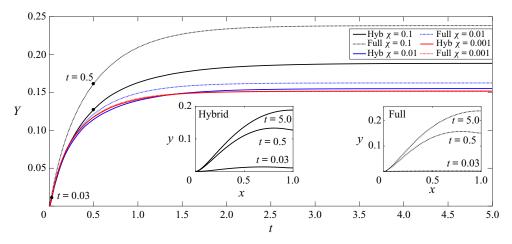

Figure 18. Comparison of the time-dependent hybrid and full model for the advancing contact line. Time signals of the meniscus rise, $Y = |y_s(s = L) - y_s(s = 0)|$, of the hybrid (solid) and full (dashed) models when $\lambda = 0.1$, $Ca = 0.2$. The different colours indicate $\chi = 0.1, 0.01, 0.001$. As the main panel shows, the system relaxes to a stable state and as $\chi \to 0$ the two models converge. The insets show interface profiles at sampled times indicated by the labels.

In our final validation calculation, we show in figure 19 that for different values of χ and θ_1 the hybrid model is consistent with the full two-layer model for variations in χ and the contact angle θ_1.
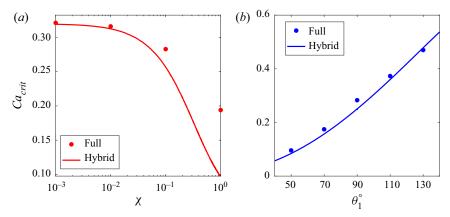
945 A34-32

Figure 19. Comparison of Ca_{crit} between hybrid (solid lines) and full (circular markers) models for the receding contact line. (*a*) Variations in χ when $\lambda = 0.1$ and $\theta_1 = \pi/2$. (*b*) Variations in θ_1 for $\lambda = \chi = 0.1$.
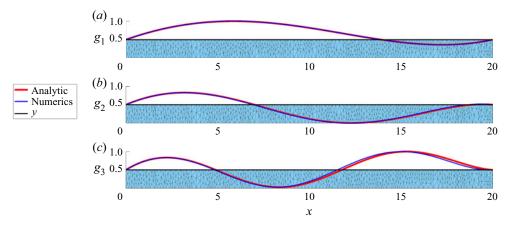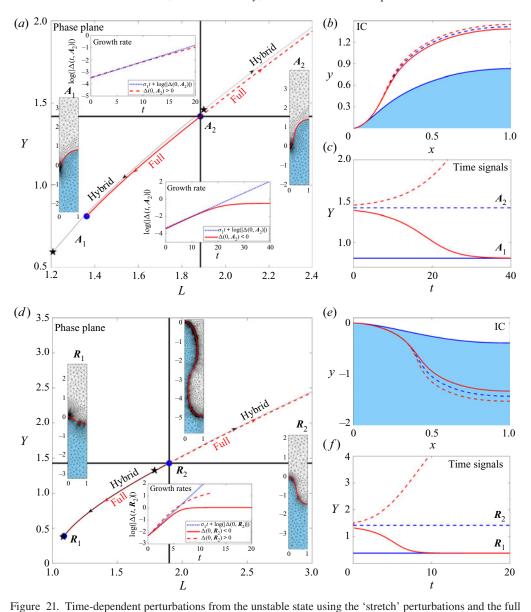

Figure 20. Comparison of eigenmodes, $H/L = 40$, $C = 3.0$. The different colour profiles indicate the analytic eigenmodes from (B2) and those obtained from the numerical calculations. (*a*) Eigenmode g_1, corresponding to the largest eigenvalue; (*b*) g_2 and (*c*) g_3 are the eigenmodes for the next two largest eigenvalues.

Appendix B. Validation of our eigenvalue analysis

We can validate the solutions of (3.5) against a situation where analytic eigenmodes are known. If we assume the plate is static ($Ca = 0$) and that $H/L \gg 1$, corresponding to a short fat pool of liquid at the bottom of the channel with no slip beneath it, then we can also apply a lubrication approximation to the liquid domain. If the fluid is treated as a vacuum we have the following equation for the vertical height of the interface:

$$y_t + C(y^3 y_{xxx})_x = 0, \tag{B1}$$

where C is a known constant containing non-dimensional system parameters (in this case we choose $C = 3$). The boundary conditions $y(0) = y(L) = y_0$, $y_{xxx}(0) = y_{xxx}(L) = 0$ describe a pinned contact line and no flux through the plates so that the resulting interface is flat in equilibrium. In this case the set of unknowns is 'one-dimensional' in that $w = [y]$ and using the perturbation in (3.3) yields a set of equations where analytic progress can

945 A34-33

Figure 21. Time-dependent perturbations from the unstable state using the 'stretch' perturbations and the full two-layer model. (*a*–*c*) Advancing contact line. (*d*–*f*) Receding contact line. (*a*,*d*) The phase plane in the (L, Y) projection, with steady states indicated by circular markers (full model) and stars (hybrid model). Trajectories that result in a stable configuration ($\Delta(t = 0, A/R_2) < 0$) are solid and those that result in a transient behaviour ($\Delta(t = 0, A/R_2) > 0$) are in dashed lines (red/full and black/hybrid). The inset diagrams show the two-layer mesh of the steady states with the interface as a solid red line, and comparisons of the growth rate of the simulations (solid/dashed red lines) and that predicted by the leading eigenvalue (dotted blue lines). In (*d*), the time-dependent state when air entrainment starts is also included. (*b*,*e*) The stable state (solid blue), unstable state (dashed blue) and the perturbations (solid/dashed red). (*c*,*f*) The time signals of each simulation. Parameter values are $\chi = 0.1$, $\lambda = 0.1$ and $Ca = 0.7$ (advancing), $Ca = 0.25$ (receding).

be made. It can be shown that the eigenvalues and eigenmodes of (B1) can be written as

$$g_n = a_n \left[\frac{\sinh(\sigma_n^{1/4}L) + \sin(\sigma_n^{1/4}L)}{\cos(\sigma_n^{1/4}L) - \cosh(\sigma_n^{1/4}L)} (\cosh(\sigma_n^{1/4}x) - \cos(\sigma_n^{1/4}x)) \right.$$
$$\left. + \sinh(\sigma_n^{1/4}x) + \sin(\sigma_n^{1/4}x) \right], \quad \sigma_n \approx \left(\frac{\pi/2 + n\pi}{L} \right)^4. \quad (B2)$$

These non-trivial analytic expressions can be used to validate our numerical stability calculations. We choose a computational domain with $H/L = 40$, to reflect $H/L \gg 1$, and calculate the corresponding eigenmodes numerically using the hybrid model described in the previous section. Figure 20 shows the first three eigenmodes corresponding to the largest three eigenmodes, $n = 1, 2, 3$, as calculated by the hybrid model and the analytic solution (different colour curves). These solutions are stable as the eigenspectra lie exclusively in the left-hand complex plane and the agreement between the numerical calculations and the analytic solution obtained from the lubrication model is excellent, giving us confidence in our computational framework.

Appendix C. Full two-layer time-dependent perturbations

In this appendix we show that the qualitative time-dependent behaviour of the full two-layer model matches that of the hybrid model. In particular we show that applying a stretch perturbation to the unstable state, as shown in § 4.1.1, leads to similar qualitative transient features. In figure 21, leading-order eigenmode perturbations, i.e. 'stretch' modes, of the unstable state in the full model result in either stable flow, if the initial interface has been contracted, or becoming transient, if the initial interface has been stretched. This qualitative behaviour precisely matches that of the hybrid model, in both the advancing and receding contact-line problems, as is evident from the red (full) and black (hybrid) curves in figure 21(*a*,*d*). Furthermore, as can be seen by the mesh in figure 21(*d*), when a thin film starts developing, the number of elements in the computational domain significantly increases due to the adapation procedure and the calculations become prohibitively expensive and eventually fail when the moving-wall contact point reaches the end of the domain, thus highlighting the attraction of the hybrid model for time-dependent simulations.

REFERENCES

AFKHAMI, S., GAMBARYAN-ROISMAN, T. & PISMEN, L.M. 2020 Challenges in nanoscale physics of wetting phenomomen. *Eur. Phys. J. Spec. Top.* **229** (10), 1735–1738.

BLAKE, T.D. 2006 The physics of moving wetting lines. *J. Colloid Interface Sci.* **299**, 1–13.

BONN, D., EGGERS, J., INDEKEU, J., MEUNIER, J. & ROLLEY, E. 2009 Wetting and spreading. *Rev. Mod. Phys.* **81** (2), 739–804.

CHAN, T.S., KAMAL, C., SNOEIJER, J.H., SPRITTLES, J.E. & EGGERS, J. 2020 Cox–Voinov theory with slip. *J. Fluid Mech.* **900**, A8.

CHAN, T.S., SNOEIJER, J.H. & EGGERS, J. 2012 Theory of the forced wetting transition. *Phys. Fluids* **24**, 072104.

CHAN, T.S., SRIVASTAVA, S., MARCHAND, A., ANDREOTTI, B., BIFERALE, L., TOSCHI, F. & SNOEIJER, J.H. 2013 Hydrodynamics of air entrainment by moving contact lines. *Phys. Fluids* **25** (7), 074105.

CHARITATOS, V., SUSZYNSKI, W.J., CARVALHO, M.S. & KUMAR, S. 2020 Dynamic wetting failure in shear-thinning and shear-thickening liquids. *J. Fluid Mech.* **892**, A1.

CHRISTODOULOU, K.N. & SCRIVEN, L.E. 1988 Finding leading modes of a viscous free surface flow: an asymmetric generalized eigenproblem. *J. Sci. Comput.* **3** (4), 355–406.

Cox, R.G. 1986 The dynamics of the spreading of liquids on a solid surface. Part 1. Viscous flow. *J. Fluid Mech.* **168**, 169–194.

Delon, G., Fermigier, M., Snoeijer, J.H. & Andreotti, B. 2007 Relaxation of a dewetting contact line. Part 2. Experiments. *J. Fluid Mech.* **579**, 63–83.

Doedel, E.J. 2007 Lecture notes on numerical analysis of nonlinear equations. In *Numerical Continuation Methods for Dynamical Systems* (ed. B. Krauskopf, H.M. Osinga & J. Galan-Vioque), pp. 1–49. Springer.

Dussan, V. 1976 The moving contact line: the slip boundary condition. *J. Fluid Mech.* **77**, 665–684.

Eckhardt, B., Faisst, H., Schmiegel, A. & Schneider, T.M. 2008 Dynamical systems and the transition to turbulence in linearly stable shear flows. *Phil. Trans. R. Soc. Lond.* A **366** (1868), 1297–1315.

Eggers, J. 2004*a* Hydrodynamic theory of forced dewetting. *Phys. Rev. Lett.* **93** (9), 094502.

Eggers, J. 2004*b* Towards a description of contact line motion at higher Capillary numbers. *Phys. Fluids* **16** (9), 3491–3494.

Eggers, J. 2005 Existence of receding and advancing contact lines. *Phys. Fluids* **17** (8), 082106.

Fernández-Toledano, J.C., Blake, T.D. & Coninck, J.D. 2021 Taking a closer look: a molecular-dynamics investigation of microscopic and apparent dynamic contact angles. *J. Colloid Interface Sci.* **587**, 311–323.

Gaillard, A., Keeler, J.S., Thompson, A.J., Hazel, A.H. & Juel, A. 2020 Life and fate of a bubble in a constricted Hele-Shaw channel. *J. Fluid Mech.* **122**, A34.

Gallino, G., Schneider, T.M. & Gallaire, F. 2018 Edge states control droplet breakup in subcritical extensional flows. *Phys. Rev. Fluids* **3**, 073603.

He, M. 2020 Long-time evolution of interfacial structure of partial wetting. *Phys. Rev. Fluids* **5** (11), 114001.

He, M. & Nagel, S.R. 2019 Characteristic interfacial structure behind a rapidly moving contact line. *Phys. Rev. Lett.* **122** (1), 018001.

Heil, M. & Hazel, A.L. 2006 oomph-lib–an object-oriented multi-physics finite-element library. In *Fluid–Structure Interaction* (ed. H.-J. Bungatz & M. Schafer), pp. 19–49. Springer.

Heroux, M., *et al.* 2003 An overview of trilinos. *Tech. Rep.* SAND2003-2927. Sandia National Laboratories.

Huh, C. & Scriven, L.E. 1971 Hydrodynamic model of steady movement of a solid/liquid/fluid contact line. *J. Colloid Interface Sci.* **35** (1), 85–101.

Jacqmin, D. 2004 Onset of wetting failure in liquid–liquid systems. *J. Fluid Mech.* **517**, 209–228.

Kamal, C., Sprittles, J.E., Snoeijer, J.H. & Eggers, J. 2019 Dynamic drying transition via free-surface cusps. *J. Fluid Mech.* **858**, 760–786.

Keeler, J.S., Blake, T.D., Lockerby, D.A. & Sprittles, J.E. 2021 Putting the micro into the macro: using a molecularly-augmented hydrodynamic model to investigate the flow instability of a liquid nano plug. *J. Fluid Mech.* arXiv:220503114.

Keeler, J.S., Thompson, A.B., Lemoult, G., Juel, A. & Hazel, A.L. 2019 The influence of invariant solutions on the transient behaviour of an air bubble in a Hele-Shaw channel. *Proc. R. Soc. Lond.* A **879**, 1–27.

Kerswell, R.R., Pringle, C.C.T. & Willis, A.P. 2014 An optimization approach for analysing nonlinear stability with transition to turbulence in fluids as an exemplar. *Rep. Prog. Phys.* **77** (8), 085901.

Krauskopf, B., Osinga, H.M., Doedel, E.J., Henderson, M.E., Guckenheimer, J., Vladimirsky, A., Dellnitz, M. & Junge, O. 2005 A survey of methods for computing (un) stable manifolds of vector fields. *Intl J. Bifurcation Chaos* **15** (03), 763–791.

Kuznetsov, Y.A. 1998 *Elements of Applied Bifurcation Theory*, 3rd edn. Springer.

Landau, L. & Levich, B. 1988 Dragging of a liquid by a moving plate. In *Dynamics of Curved Fronts* (ed. P. Pelcé), pp. 141–153. Elsevier.

Ledesma-Aguilar, R., Nistal, R., Hernández-Machado, A. & Pagonabarraga, I. 2011 Controlled drop emission by wetting properties in driven liquid filaments. *Nat. Mater.* **10**, 367–371.

Li, X.S. 2005 An overview of superlu: algorithms, implementation, and user interface. *ACM Trans. Math. Soft. (TOMS)* **31** (3), 302–325.

Liu, C.-Y., Carvalho, M.S. & Kumar, S. 2017 Mechanisms of dynamic wetting failure in the presence of soluble surfactants. *J. Fluid Mech.* **825**, 677–703.

Liu, C.-Y., Carvalho, M.S. & Kumar, S. 2019 Dynamic wetting failure in curtain coating: comparison of model predictions and experimental observations. *Chem. Engng Sci.* **195**, 74–82.

Liu, C.-Y., Vandre, E., Carvalho, M.S. & Kumar, S. 2016*a* Dynamic wetting failure and hydrodynamic assist in curtain coating. *J. Fluid Mech.* **808**, 290–315.

Liu, C.-Y., Vandre, E., Carvalho, M.S. & Kumar, S. 2016*b* Dynamic wetting failure in surfactant solutions. *J. Fluid Mech.* **789**, 285–309.

Marchand, A., Chan, T.S., Snoeijer, J.H. & Andreotti, B. 2012 Air entrainment by contact lines of a solid plate plunged into a viscous fluid. *Phys. Rev. Lett.* **108** (20), 204501.

ORON, A., DAVIS, H.S. & BANKOFF, G.S. 1997 Long-scale evolution of thin liquid films. *Rev. Mod. Phys.* **69** (3), 931–980.

PACK, M., KANEELIL, P., KIM, H. & SUN, Y. 2018 Contact line instability caused by air rim formation under nonsplashing droplets. *Langmuir* **34** (17), 4962–4969.

REYSATT, E. & QUÉRÉ, D. 2006 Bursting of a fluid film in a viscous environment. *Europhys. Lett.* **73**, 236–247.

SACKINGER, P.A., SCHUNK, P.R. & RAO, R.R. 1996 A Newton–Raphson pseudo-solid domain mapping technique for free and moving boundary problems: a finite element implementation. *J. Comput. Phys.* **125** (1), 83–103.

SBRAGAGLIA, M., SUGIYAMA, K. & BIFERALE, L. 2008 Wetting failure and contact line dynamics in a Couette flow. *J. Fluid Mech.* **614**, 471–493.

SEMENOV, S., STAROV, V.M., VELARDE, M.G. & RUBIO, R.G. 2011 Droplets evaporation: problems and solutions. *Eur. Phys. J. Spec. Top.* **197** (1), 265–278.

SEVERTSON, Y.C. & AIDUN, C.K. 1996 Stability of two-layer stratified flow in inclined channels: applications to air entrainment in coating systems. *J. Fluid Mech.* **312**, 173–200.

SHIKHMURZAEV, Y.D. 2006 Singularities at the moving contact line, mathematical, physical and computational aspects. *Physica* D **217** (2), 121–133.

SHIKHMURZAEV, Y.D. 2007 *Capillary Flows with Forming Interfaces*. CRC Press.

SNOEIJER, J.H. & ANDREOTTI, B. 2013 Moving contact lines: scales, regimes, and dynamical transitions. *Annu. Rev. Fluid Mech.* **45**, 269–292.

SNOEIJER, J.H., ANDREOTTI, B., DELON, G. & FERMIGIER, M. 2007 Relaxation of a dewetting contact line. Part 1. A full-scale hydrodynamic calculation. *J. Fluid Mech.* **579**, 63–83.

SNOEIJER, J.H., DELON, G., ANDREOTTI, B. & FERMIGIER, M. 2006 Avoided critical behavior in dynamically forced wetting. *Phys. Rev. Lett.* **96**, 174504.

SNOEIJER, J.H., ZIEGLER, J., ANDREOTTI, B., FERMIGIER, M. & EGGERS, J. 2008 Thick films of viscous fluid coating a plate withdrawn from a liquid reservoir. *Phys Rev. Lett.* **100** (24), 244502.

SPRITTLES, J.E. 2015 Air entrainment in dynamic wetting: Knudsen effects and the influence of ambient air pressure. *J. Fluid Mech.* **769**, 444–481.

SPRITTLES, J.E. 2017 Kinetic effects in dynamic wetting. *Phys. Rev. Lett.* **118** (11), 114502.

SPRITTLES, J.E. & SHIKHMURZAEV, Y.D. 2011*a* Viscous flow in domains with corners: numerical artifacts, their origin and removal. *Comput. Meth. Appl. Mech. Engng* **200** (9–12), 1087–1099.

SPRITTLES, J.E. & SHIKHMURZAEV, Y.D. 2011*b* Viscous flows in corner regions: singularities and hidden eigensolutions. *Intl J. Numer. Meth. Fluids* **65** (4), 372–382.

SPRITTLES, J.E. & SHIKHMURZAEV, Y.D. 2013 Finite element simulation of dynamic wetting flows as an interface formation process. *J. Comput. Phys.* **233**, 34–65.

STAY, M.S. & BAROCAS, V.H. 2003 Coupled lubrication and Stokes flow finite elements. *Intl J. Numer. Meth. Fluids* **42**, 129–146.

THORODDSEN, S.T., THORAVAL, M.-J., TAKEHARA, K. & ETOH, T.G. 2012 Micro-bubble morphologies following drop impacts onto a pool surface. *J. Fluid Mech.* **708**, 469–479.

VANDRE, E. 2013 Onset of dynamic wetting failure: The mechanics of high-speed fluid displacement. PhD thesis, University of Minnesota, USA.

VANDRE, E., CARVALHO, M.S. & KUMAR, S. 2012 Delaying the onset of dynamic wetting failure through meniscus confinement. *J. Fluid Mech.* **707**, 496–520.

VANDRE, E., CARVALHO, M.S. & KUMAR, S. 2013 On the mechanism of wetting failure during fluid displacement along a moving substrate. *Phys. Fluids* **25**, 102013.

VOINOV, O.V. 1976 Hydrodynamics of wetting. *Fluid Dyn.* **11**, 714–721.

ZIENKIEWICZ, O.C. & ZHU, J.Z. 1992 The superconvergent patch recovery and a posteriori error estimates. Part 1: the recovery technique. *Intl J. Numer. Meth. Engng* **33** (7), 1331–1364.